

Architectures of Exoplanetary Systems. II: An Intrinsic Relation between Planetary System Occurrence and Spectral Type for Kepler’s FGK Dwarfs

Matthias Y. He^{1,2,3,4*}, Eric B. Ford^{1,2,3,4}, and Darin Ragozzine⁵

¹Department of Astronomy and Astrophysics, 525 Davey Laboratory, The Pennsylvania State University, University Park, PA 16802, USA

²Center for Exoplanets and Habitable Worlds, 525 Davey Laboratory, The Pennsylvania State University, University Park, PA 16802, USA

³Center for Astrostatistics, 525 Davey Laboratory, The Pennsylvania State University, University Park, PA 16802, USA

⁴Institute for Computational & Data Sciences, The Pennsylvania State University, University Park, PA 16802, USA

⁵Department of Physics and Astronomy, N283 ESC, Brigham Young University, Provo, UT 84602, USA

Accepted ?. Received ?; in original form ?

ABSTRACT

The *Kepler* mission observed thousands of transiting exoplanet candidates around hundreds of thousands of FGK dwarf stars. He, Ford, & Ragozzine (2019) applied forward modelling to infer the distribution of intrinsic architectures of planetary systems, developed a clustered Poisson point process model for exoplanetary systems (SysSim) to reproduce the marginal distributions of the observed *Kepler* population, and showed that orbital periods and planet radii are clustered within a given planetary system. Here, we extend the clustered model to explore correlations between planetary systems and their host star properties. We split the sample of Kepler FGK dwarfs into two halves and model the fraction of stars with planets (between 0.5 – 10 R_{\oplus} and 3–300 d), f_{swpa} , as a linear function of the Gaia DR2 $b_p - r_p$ color. We find that the occurrence of these planets rises significantly towards later type (redder or higher $b_p - r_p$) stars, with a slope of $df_{\text{swpa}}/d(b_p - r_p) = 0.53^{+0.19}_{-0.19}$. The fraction of stars with planets increases from $f_{\text{swpa}} = 0.34^{+0.08}_{-0.11}$ for F2V dwarfs to $f_{\text{swpa}} = 0.91^{+0.09}_{-0.18}$ for mid K-dwarfs. About half ($f_{\text{swpa}} = 0.54^{+0.08}_{-0.13}$) of all solar-type (G2V) dwarfs harbour a planetary system between 3 and 300 d. While this linear $f_{\text{swpa}}(b_p - r_p)$ model is simple, it can closely match the observed multiplicity distributions of both bluer and redder halves in our sample, suggesting that the architectures of planetary systems around stars of different spectral types may be similar aside from a shift in the overall fraction of planet hosting stars.

Key words: methods: statistical – planetary systems – planets and satellites: detection, fundamental parameters, terrestrial planets – stars: statistics

1 INTRODUCTION

NASA’s *Kepler* mission (Borucki et al. 2010, 2011a,b; Batalha et al. 2013) boosted the number of strong exoplanet candidates by surveying $\sim 200,000$ stars for nearly four years. It revealed a large number of transiting super-Earth to sub-Neptune size planets ($R_p \lesssim 4R_{\oplus}$) at short orbital periods ($P \lesssim 1$ yr) (Latham et al. 2011; Lissauer et al. 2011a,b, 2014; Rowe et al. 2014) and an abundance of tightly-spaced multitransiting planetary systems. These offer key clues about their architectures and formation histories (Ragozzine & Holman 2010; Fabrycky et al. 2014; Winn & Fabrycky 2015; He, Ford, & Ragozzine 2019). In addition to enabling robust calculations of the planet population statistics themselves, the *Kepler*

catalogue also allows for the detailed study of the correlations between planetary systems and their host stars.

Many previous studies have used the census of exoplanet candidates from *Kepler* to infer the occurrence rates of planets around primarily main sequence stars of F, G, and K spectral types (Catanzarite & Shao 2011; Howard et al. 2012; Fressin et al. 2013; Petigura, Marcy, & Howard 2013b; Hsu et al. 2018; Mulders et al. 2018; Hsu et al. 2019). Of these studies, Howard et al. (2012) was the first to report a dependence of the planet occurrence rate on host star spectral type. They used 1235 planet candidates (with orbital periods < 50 d) from the first three quarters of *Kepler* data (Borucki et al. 2011b), around dwarf stars spanning $T_{\text{eff}} = 3600 - 7100$ K, to explore how the occurrence of planets varies as a function of stellar effective temperature. By splitting the stellar sample into 500 K bins, they found a strong inverse relationship between the occurrence of small ($R_p = 2 - 4R_{\oplus}$) planets and T_{eff} , for which they fit a linear model,

* Contact e-mail: myh7@psu.edu

$f(T_{\text{eff}}) = f_0 + k_T(T_{\text{eff}} - 5100\text{K})/1000\text{K}$ where $f_0 = 0.165 \pm 0.011$ and $k_T = -0.081 \pm 0.011$. Interestingly, they did not find any such correlation for larger planets ($R_p = 4 - 32R_{\oplus}$).

In contrast, [Fressin et al. \(2013\)](#) found no dependence between planet occurrence and spectral type for the same planet sizes, using the first 16 quarters of the *Kepler* data containing ~ 2300 planet candidates ([Batalha et al. 2013](#)) combined with a new model for the detection efficiency and accounting for false positives. They argue that the increase in planet occurrence towards later type stars is a result of observational bias, manifesting due to three reasons: 1) the *Kepler* planet candidate list is incomplete for sub-Neptunes, such that many of these planets transiting the larger (earlier type) stars have not been recovered, 2) the distribution of planet radii rises towards smaller sizes, which are easier to detect around smaller (later type) stars, and 3) the false positive rate is slightly higher for later-type stars, artificially boosting the occurrence rate if not corrected for. In this work, we are able to address these concerns by taking advantage of more recent improvements in modelling *Kepler*'s detection efficiency ([Burke & Catanzarite 2017a,b,c](#); [Christiansen 2017](#); [Coughlin 2017](#)), including accounting for the rate of false positives from the *Robovetter* and using the *Kepler* DR25 catalogue that was vetted using this fully automated pipeline ([Thompson et al. 2018](#)). We show that the limit of transit detectability for a given planet is more complicated than what would result from only considering the stellar radius.

[Mulders, Pascucci, & Apai \(2015\)](#) extended the above studies to include a large sample of F, G, K, and M dwarfs, dividing these four spectral types using T_{eff} and computing the planet occurrence rates in each bin. With an eye towards exploring how the planetary system architectures, not just the overall rate of planets, may differ across stellar types, they calculated the occurrence rate as a function of semi-major axis, for each spectral type. They find that the occurrence rate of planets between $1 - 4R_{\oplus}$ increases towards later spectral type at all separations out to ~ 150 d, in agreement with the findings of [Howard et al. \(2012\)](#). [Mulders, Pascucci, & Apai \(2015\)](#) also suggest that the cut-off semi-major axis (potentially indicative of the inner disk edge, where planets become less common interior of) shifts towards smaller separations for planets around later type stars.

The occurrence rates of planets around M-dwarf stars have also been estimated by [Dressing & Charbonneau \(2013\)](#), who used a sample of ~ 3900 stars then estimated to have $T_{\text{eff}} < 4000$ K hosting 95 planet candidates. Their results for the occurrence rates of small planets are generally larger than the values for FGK dwarfs found by other studies. Intriguingly, however, they find that the occurrence of planets ($R_p = 1.4 - 4R_{\oplus}$) may actually increase from the cooler (mid) to hotter (early) M-dwarfs, although the number of planet candidates driving this result is relatively small (and they find no such trend for smaller planets $R_p = 0.5 - 1.4R_{\oplus}$). More recently, [Hardegree-Ullman et al. \(2019\)](#) also find an increased occurrence rate of planets around M-dwarfs, although with much larger uncertainties, as well as evidence for an increasing occurrence towards later M-dwarfs. The higher occurrence of planets around M-dwarfs has also been suggested by [Gaidos et al. \(2016\)](#), who estimated an average of 2.2 ± 0.3 planets ($R_p = 1 - 4R_{\oplus}$) per star between 1.5–180 d. Finally, [Hsu, Ford, & Terrien \(2020\)](#) and [Bryson \(2020\)](#) leveraged *Kepler* DR25, *Gaia* DR2, and 2MASS data to compute the planet occurrence rates around M-dwarfs. While their findings corroborate these previous results, they also show that the increased occurrence rates compared to that of FGK stars largely disappears when normalizing by stellar irradiance.

At the time of writing this paper, [Yang, Xie, & Zhou \(2020\)](#) also

used the *Kepler* DR25 catalog of exoplanet candidates to study the occurrence of planetary systems, namely the fraction of stars with planets, as a function of stellar type. They split a sample of stars between 3000–7500 K into ten quantiles and modelled the fraction of stars with planets, the mean planet multiplicity, and the mutual inclination dispersion power-law index α (assuming the same mutual inclination σ_i –planet multiplicity k relation from [Zhu et al. 2018](#), $\sigma_i \propto k^\alpha$) in each quantile. They also find that the fraction of stars with planets, and to a lesser significance, the mean number of planets per system, increases with decreasing stellar effective temperature. In this paper, we take a similar approach as [Yang, Xie, & Zhou \(2020\)](#) to focus on the fraction of stars with planets as opposed to just the mean number of planets per star, as both of these quantities can be computed given knowledge of the intrinsic planet multiplicity distribution, which we constrain using our forward model. We extend the methodology described in [He, Ford, & Ragozzine \(2019\)](#) (hereafter [Paper I](#)) to explore a clustered model describing the relation between planetary architectures and host star properties, using *Gaia* $b_p - r_p$ colors as a proxy for stellar effective temperature (and equivalently, spectral type). We summarize our forward modelling procedure in §2, focusing on the key features and updates while leaving the full details in [Paper I](#) (§2 therein). We model the fraction of stars with planets as a linear function of $b_p - r_p$ for our FGK sample and show that the occurrence of planetary systems increases significantly towards later type stars. In §3, we present our results for our new clustered models. We discuss the implications of our results in §4. Finally, we summarize our conclusions in §5.

2 METHODS

As in [Paper I](#) (and described therein), our models are built in the context of the Exoplanets Systems Simulator (“SysSim”) codebase, which can be installed as the ExoplanetsSysSim.jl package ([Ford et al. 2018b](#)). Step-by-step instructions on how to install, as well as our forward models, can be accessed at <https://github.com/ExoJulia/SysSimExClusters>. The SysSim project is also described in [Hsu et al. \(2018, 2019\)](#).

Our previous models for planetary systems (a non-clustered, clustered periods, and clustered periods and sizes model) and our multi-stage approach to performing an approximate Bayesian computing (ABC) analysis are fully described in [Paper I](#). Here, we modify our best model, the clustered periods and sizes model, to explore the dependence on host star properties. In this section, we first summarize our full procedure and then describe the updates:

Step 0: Define a statistical description for the intrinsic distribution of exoplanetary systems.

Step 1: Generate an underlying population of exoplanetary systems (*physical catalogue*).

Step 2: Generate an observed population (*observed catalogue*) from the *physical catalogue*.

Step 3: Compare the simulated *observed catalogue* with the *Kepler* data.

Step 4: Optimize a distance function to find the best-fit model parameters.

Step 5: Explore the posterior distribution of model parameters using a Gaussian Process (GP) emulator.

Step 6: Compute credible intervals for model parameters and simulated catalogues using ABC.

Our updates to each step are described in the following subsections.

2.1 Clustered model updates

In [Paper I](#), we explored three models simulating planetary systems as a clustered Poisson point process and used forward modelling to fit to the key properties (e.g., marginal distributions of the principal observables for detected planets) of the *Kepler* planet catalogue around a clean sample of FGK stars ([Hsu et al. 2019](#)). We found that the occurrence of multi-transiting systems, and their distributions of period ratios and radius ratios are highly clustered to an extent that a simple non-clustered model cannot reproduce. We showed that instead, a model involving clustered periods and planet sizes provides the best fit to the observed data.

In this paper, we adopt this fully clustered model from [Paper I](#) and modify it slightly with a re-parametrization, before adding a dependence on the host star colour. To review, our clustered periods and sizes model as described in [Paper I](#) consists of the following features:

Planet clusters: each planetary system is composed of “clusters” of planets. We attempt to assign a number of clusters drawn from a Poisson distribution (with mean parameter λ_c), but some may be rejected due to stability concerns (see §2.2 of [Paper I](#) for the exact procedure). The number of planets for each cluster is drawn from a zero-truncated Poisson (ZTP) distribution (with mean parameter λ_p).

Orbital periods: a power-law (with slope index α_P) describes the distribution of cluster period scales P_c , and the period of each planet in the cluster is drawn from a log-normal distribution centred on P_c with cluster width $N_p \sigma_P$ (where N_p is the number of planets in the cluster and σ_P is a width scale parameter), between 3 and 300 d.

Planet radii: a broken power-law (with slope indices α_{R1} , α_{R2} , and break radius $R_{p,\text{break}} = 3R_\oplus$) describes the distribution of cluster radius scales $R_{p,c}$, and the radius of each planet in the cluster is drawn from a log-normal distribution centred on $R_{p,c}$ with cluster width σ_R , between 0.5 and $10R_\oplus$.

Planet masses: a non-parametric, probabilistic mass–radius relation from [Ning, Wolfgang, & Ghosh \(2018\)](#) is used to draw the masses of the planets conditioned on their radii.

Eccentricities: the orbital eccentricities are drawn from a Rayleigh distribution (with scale σ_e).

Mutual inclinations: two Rayleigh distributions for the mutual inclinations are used, corresponding to a high and a low mutual inclination population (with scales $\sigma_{i,\text{high}}$ and $\sigma_{i,\text{low}}$, respectively, such that $\sigma_{i,\text{high}} \geq \sigma_{i,\text{low}}$), where the fraction of systems belonging to the high inclination population is $f_{\sigma_{i,\text{high}}}$.

Planets near resonance: peaks near the first-order mean motion resonances (MMRs) in the observed period ratio distribution are produced by drawing low mutual inclinations for the planets “near an MMR” with another planet (which we define as cases where the period ratio is in the range $[\mathcal{P}_{\text{mmr}}, 1.05\mathcal{P}_{\text{mmr}}]$ for any \mathcal{P}_{mmr} in $\{2:1, 3:2, 4:3, 5:4\}$), such that these planets have mutual inclinations

drawn from the Rayleigh distribution with $\sigma_{i,\text{low}}$ regardless of which mutual inclination population the system belongs to.

Stability criteria: adjacent planets are separated by at least $\Delta_c = 8$ mutual Hill radii, and orbital periods are resampled until this criteria is met. For clusters where all a maximum number of resampling attempts has been met, the entire cluster is discarded.

2.1.1 Modified clustered model: constant f_{swpa}

The model described above induces a link between the way planets are distributed between clusters and the number of zero planet systems, since the number of clusters per system is drawn from a Poisson distribution which also controls the number of zero-cluster (and thus zero-planet) draws. To decouple these two, we modify the model by introducing an additional parameter, the fraction of stars with planets attempted f_{swpa} , and replace the Poisson distribution for the number of clusters per system with also a zero-truncated Poisson. This way, f_{swpa} controls the fraction of stars we draw planetary systems for, while λ_c and λ_p both parametrize the (ZTP-distributed) numbers of clusters and planets per cluster, respectively, for such systems. We call f_{swpa} the fraction of stars with planets *attempted* because systems for which we draw planets can still end up with zero planets in the case where all planets are discarded after the maximum number of attempts due to the stability criteria, although this is very unlikely.

We make this modification to our clustered periods and sizes model from [Paper I](#) not only to decouple the number of zero-planet systems from the underlying multiplicity distribution, but to also serve as a baseline model for a more natural comparison to the new model we introduce below. For the remainder of this paper, we refer to this baseline model as the clustered model with constant f_{swpa} .

In [Figure 1](#), we plot the intrinsic distributions of total planet multiplicity, clusters per system N_c , and planets per cluster N_p , for our old clustered model from [Paper I](#) (red dotted line) and our constant f_{swpa} model (green dashed line). While our parametrization is different between these models, we find that the resulting intrinsic planet multiplicity distribution is very similar (top panel). We discuss these results in more detail in §3.1.

2.1.2 Generalized clustered model: linear $f_{\text{swpa}}(b_p - r_p)$ dependence on host star colour

The occurrence of planetary systems is perhaps not independent of the host star properties ([Howard et al. 2012](#); [Dressing & Charbonneau 2013](#); [Mulders, Pascucci, & Apai 2015](#)). As we motivate in §3, we find that while our clustered periods and sizes model performs well for our sample of *Kepler* planetary systems around FGK stars as a whole ([Paper I](#)), there are differences in the way these planets are distributed for different stars. These differences are complicated by the complex detection biases present in the *Kepler* survey. Since we are forward modelling planetary systems in detail using SysSim, our approach allows us to test various models in order to distinguish between these observational effects and real trends in the data.

In order to account for the potential differences in planet occurrence as a function of stellar properties, we introduce a host-star dependence in our clustered model. We assume the form of a simple, linear relation between the fraction of stars with planets (i.e.,

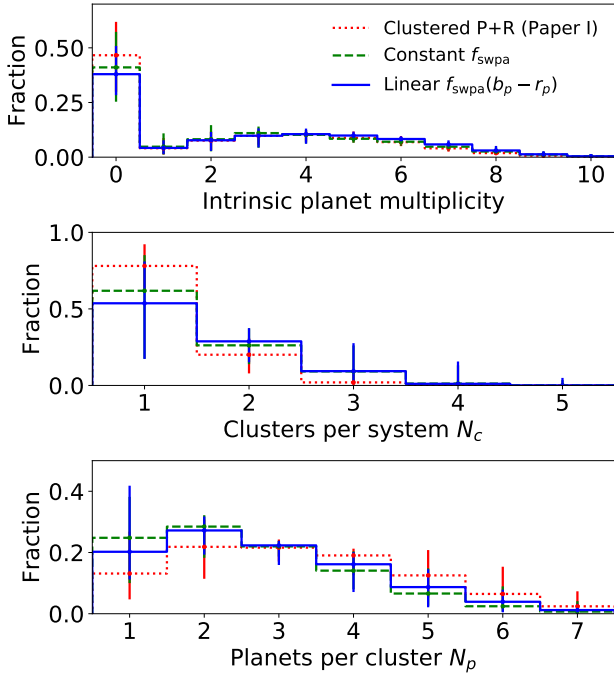


Figure 1. Intrinsic distributions of total planet multiplicity (top panel), cluster multiplicity N_c (middle panel), and planets per cluster N_p (bottom panel) drawn from our models. In [Paper I](#), our clustered models (red dotted line) are parametrized by $\text{Poisson}(\lambda_c)$ and zero-truncated $\text{Poisson}(\lambda_p)$ distributions for N_c and N_p , respectively. Thus, zero-planet systems result from draws of $N_c = 0$. In this paper, we parametrize our constant f_{swpa} model (green dashed line) and linear $f_{\text{swpa}}(b_p - r_p)$ model (blue solid line) with ZTP distributions for both N_c and N_p , with a separate parameter for the overall fraction of stars with planets f_{swpa} (so zero-planet systems make up $1 - f_{\text{swpa}}$ of all systems). Error bars denote the 68% credible regions computed from 100 catalogues passing our KS distance threshold for each model. While our new parametrization results in somewhat more clusters per system and fewer planets per cluster, the total planet multiplicity distribution is very similar between all three models. In particular, the (overall) fraction of stars with planets is well constrained in all three models.

f_{swpa}) and the stellar colour ($b_p - r_p$ from *Gaia*):

$$f_{\text{swpa}}(b_p - r_p) = \max \left\{ 0, \min \left[m \left((b_p - r_p) - (b_p - r_p)_{\text{med}} \right) + f_{\text{swpa, med}}, 1 \right] \right\} \quad (1)$$

where $m = \frac{df_{\text{swpa}}}{d(b_p - r_p)}$ is the slope of the line, and $f_{\text{swpa, med}} = f_{\text{swpa}}((b_p - r_p)_{\text{med}})$ is the y-intercept (which we have chosen to parametrize at the median colour, $(b_p - r_p)_{\text{med}}$). For our stellar sample (as defined in [Hsu et al. 2019](#) and described in [Paper I](#)), the median colour is $(b_p - r_p)_{\text{med}} \approx 0.95$ mag. We enforce $f_{\text{swpa}}(b_p - r_p)$ to be bounded between 0 and 1, since the fraction of systems with planets cannot be negative or greater than 1. We refer to this model as the clustered model with linear $f_{\text{swpa}}(b_p - r_p)$. Our previous (baseline) model is essentially a special case of this more general model, where the slope is set to $m = \frac{df_{\text{swpa}}}{d(b_p - r_p)} = 0$.

The blue solid lines in [Figure 1](#) show the intrinsic planet and cluster multiplicity distributions for this linear $f_{\text{swpa}}(b_p - r_p)$ model. While the fraction of stars with planets (and thus the fraction of zero-planet systems) is a strong function of host star colour as we will show in [§3](#), the intrinsic planet multiplicity distribution

marginalized over all the FGK stars in our sample are virtually identical to that of our baseline model (constant f_{swpa} ; green dashed line). Moreover, the distributions of the numbers of clusters per planetary system and planets per cluster are also the same between these two models, and are *not* host star dependent since we have not made λ_c or λ_p functions of $b_p - r_p$.

2.2 Observational comparisons

We adopt the same procedure for constraining our model parameters as described in [Paper I](#), by defining a similar set of summary statistics and a distance function that accounts for these summary statistics.

2.2.1 Summary statistics

Since we are interested in how planet occurrence varies as a function of stellar colour, we divide the stellar sample into two halves, split at the median $b_p - r_p$ colour (a “bluer” half, with smaller $b_p - r_p$ values, and a “redder” half, with larger $b_p - r_p$ values). We compute the same summary statistics for each half, in addition to the full sample (hereafter labeled as “All”), for each observed catalogue:

- (i) the total number of observed planets $N_{p, \text{tot}}$ relative to the number of target stars N_{stars} , $f = N_{p, \text{tot}}/N_{\text{stars}}$,
- (ii) the observed multiplicity distribution, $\{N_m\}$, where N_m is the number of systems with m observed planets and $m = 1, 2, 3, \dots$,
- (iii) the observed orbital period distribution, $\{P\}$,
- (iv) the observed period ratio distribution, $\{\mathcal{P}\}$,
- (v) the observed transit depth distribution, $\{\delta\}$,
- (vi) the observed transit depth ratio distribution, $\{\delta_{i+1}/\delta_i\}$,
- (vii) the observed transit duration distribution, $\{t_{\text{dur}}\}$,
- (viii) the observed period-normalized transit duration ratio distribution of adjacent planets apparently near an MMR, $\{\xi_{\text{res}}\}$, and not near an MMR, $\{\xi_{\text{non-res}}\}$. The normalized transit duration ratio is given by $\xi = (t_{\text{dur, in}}/t_{\text{dur, out}})(P_{\text{out}}/P_{\text{in}})^{1/3}$ ([Steffen et al. 2010](#); [Fabrycky et al. 2014](#)).

The list above contains nine summary statistics, which we compute for each full observed catalogue as well as for each of the bluer and redder halves, totaling 27 summary statistics.

2.2.2 Distance function

In [Paper I](#), we used a linear weighted sum of individual distance terms to combine the fits to each summary statistic into a single distance function. Two separate distance functions were used for the analysis, with one adopting the two-sample Kolmogorov–Smirnov (KS; [Kolmogorov 1933](#); [Smirnov 1948](#)) distance for each marginal distribution and the other adopting a modified version of the two-sample Anderson–Darling (AD; [Anderson & Darling 1952](#); [Pettitt 1976](#); see equations 23–24 in [Paper I](#) for our modification) statistic. Both distance functions included a term for the overall rate of planets ($D_f = |f_{\text{sim}} - f_{\text{Kepler}}|$, where $f_{\text{sim}} = N_{p, \text{tot}}/N_{\text{stars}}$ and likewise for *Kepler*) and the observed multiplicity distribution ($D_{\text{mult}} = \rho_{\text{CRPD}} = (9/5) \sum_j O_j [(O_j/E_j)^{2/3} - 1]$, where O_j are the numbers of “observed” systems in our models and E_j are the numbers of expected systems from the *Kepler* data, for multiplicity bins $j = 1, 2, 3, 4, 5+$; see [Cressie & Read 1984](#) and the discussion surrounding equation 19 in [Paper I](#)).

For this paper, we extend the distance function in the same way as the summary statistics, by computing the individual distance

Table 1. Weights for the individual distance terms as computed from a reference clustered periods and sizes model (from Paper I, with the chosen set of parameters listed in Table 3). Each weight w is computed as the inverse of the root mean square of the distances $\hat{\sigma}(\mathcal{D})$ between repeated realizations of the same (i.e. “perfect”) model, $w = 1/\hat{\sigma}(\mathcal{D})$, using the same number of target stars as our *Kepler* sample. The weights are shown here as rounded whole numbers for guidance purposes only.

Distance term	All		Bluer		Redder	
	$\hat{\sigma}(\mathcal{D})$	w	$\hat{\sigma}(\mathcal{D})$	w	$\hat{\sigma}(\mathcal{D})$	w
D_f	0.00102	983	0.00159	627	0.00137	727
D_{mult}	0.00686	146	0.01223	82	0.01583	63
\mathcal{D}_{KS} :						
$\{P\}$	0.02937	34	0.03798	26	0.04372	23
$\{P\}$	0.05197	19	0.06681	15	0.08109	12
$\{\delta\}$	0.03049	33	0.0406	25	0.04568	22
$\{\delta_{i+1}/\delta_i\}$	0.04993	20	0.06196	16	0.08118	12
$\{t_{\text{dur}}\}$	0.02953	34	0.0375	27	0.04381	23
$\{\xi_{\text{res}}\}$	0.11414	9	0.14618	7	0.19099	5
$\{\xi_{\text{non-res}}\}$	0.05629	18	0.07268	14	0.08478	12
\mathcal{D}_{AD} :						
$\{P\}$	0.00152	659	0.00249	402	0.00322	311
$\{P\}$	0.00409	245	0.00684	146	0.0105	95
$\{\delta\}$	0.00177	566	0.00289	345	0.00392	255
$\{\delta_{i+1}/\delta_i\}$	0.00365	274	0.00545	183	0.01019	98
$\{t_{\text{dur}}\}$	0.00171	585	0.00251	399	0.00336	297
$\{\xi_{\text{res}}\}$	0.02096	48	0.03348	30	0.06504	15
$\{\xi_{\text{non-res}}\}$	0.00463	216	0.00758	132	0.01103	91

term corresponding to each summary statistic, for each of the bluer, redder, and full samples, and summing them using a set of weights $w_{i'}$.

$$\mathcal{D}_W = \sum_{\text{samples}} \sum_{i'} w_{i'} \mathcal{D}_{i'} \quad (2)$$

$$= \sum_{\text{samples}} \left[\frac{D_f}{\hat{\sigma}(D_f)} + \frac{D_{\text{mult}}}{\hat{\sigma}(D_{\text{mult}})} + \sum_{i=1}^7 \frac{\mathcal{D}_i}{\hat{\sigma}(\mathcal{D}_i)} \right], \quad (3)$$

where $w_{i'} = 1/\hat{\sigma}(\mathcal{D}_{i'})$ and everything within the outer summation refer to the distances computed using the summary statistics in a given sample only. The distances \mathcal{D}_i within the inner summation are either KS or AD distances, where the summation is over the indices labeling the summary statistics (iii)–(viii).

Old weights: In order to compute the weights in Paper I, a single reference catalogue was generated (using a nominal set of model parameters for the clustered periods and sizes model, and the same number of targets as our *Kepler* sample) and 1000 repeated catalogues were simulated (with five times as many targets, to reduce stochastic noise) from the same (i.e. “perfect”) model. The summary statistics and distances were then computed for each of the 1000 catalogues compared to the reference catalogue, and the weight for each distance term was taken as the reciprocal of the root mean square (RMS) of that distance term, $w_i = 1/\hat{\sigma}(\mathcal{D}_i)$, where \mathcal{D}_i is the i^{th} distance term, and $\hat{\sigma}$ is the RMS. While the weights computed in this way are reasonable, we find that they are prone to stochastic noise, even with larger numbers of repeated catalogues, since this method essentially treats one realization of the “perfect” model as the true data (i.e., the one used as the reference catalogue). Also, the use of five times the number of targets for the repeated catalogues inflates the weights, due to reduced Monte Carlo noise and thus smoother distributions of the summary statistics.

New weights: In this study we compute the weights in a revised manner to resolve both of the above points: we simulate 100 catalogues assuming a single model, each with the same number of targets as the *Kepler* sample, and then compute the individual distances for each unique pair of catalogues before computing the RMS for each distance term. This way, each of the 100 realizations of the same model are treated equally, with no single catalogue serving as *the* reference catalogue (or equivalently, *all* the catalogues serve as the reference catalogue), and there are effectively more evaluations of each distance term¹. We find that the weights generated in this way are significantly more reliable, even with the reduced number of model evaluations. The RMS distances and weights are listed in Table 1. We also use a set of best-fitting model parameters from Paper I for the reference catalogue (the parameters are listed in Table 3).

2.2.3 The *Kepler* catalogue

We use the exact same stellar and planetary catalogue from Paper I (see §2.4.3 therein), and briefly summarize the sample here. The stellar catalogue is derived from Hsu et al. (2019) (see §3.1 therein) and involves a series of cuts on the *Kepler* DR25 target list based on updated stellar parameters from the *Gaia* DR2 (Gaia Collaboration et al. 2018), resulting in a clean sample of 79,935 FGK main-sequence stars. We also adopt the cross-matched *Gaia* $b_p - r_p$ colours, central to the analyses in this paper. These colours range from $b_p - r_p \simeq 0.5$ (\sim F2V) at the bluest end to $b_p - r_p \simeq 1.7$ (\sim K7V) at the reddest end. The planet catalogue is derived from the *Kepler* DR25 KOI table (only keeping planet candidates around stars in our stellar catalogue), where we:

- (i) replace the transit depths and durations with the median values from the posterior samples in Rowe et al. (2015),
- (ii) replace the planet radii based on the transit depths and the updated *Gaia* DR2 stellar radii, and
- (iii) only keep planets in the period range [3, 300] d and planet radii range $[0.5, 10]R_{\oplus}$.

2.3 Model optimization

We adopt the same multi-stage approach in Paper I for performing approximate Bayesian inference on our model parameters. Our forward model is complex and relatively expensive, taking ~ 10 s to generate a physical and observed catalogue with the same number of targets as our *Kepler* catalogue. The model is also stochastic due to Monte Carlo noise and the finite catalogue size, resulting in a noisy distance function even for repeated evaluations using the exact same model parameters. Finally, the parameter space we are optimizing over is large, even larger than that of our clustered periods and sizes model due to the introduction of the f_{swpa} parameter for our baseline model, and $f_{\text{swpa,med}}$ and $d_{f_{\text{swpa}}}/d(b_p - r_p)$ for our linear $f_{\text{swpa}}(b_p - r_p)$ model. Thus, we begin with an optimization stage before training and using a fast emulator for inference with ABC.

¹ With just 100 simulated catalogues, each distance term is computed $\binom{100}{2} = 4950$ times instead of 1000 as before.

Table 2. Optimizer bounds (i.e. search ranges during the optimization stage), GP length scale hyperparameters λ_i , and emulator bounds for each free parameter of the models. The same values are used for both the analyses involving the KS and AD distance terms. The optimization bounds are larger than the emulator bounds since the initial stage involves simply exploring the parameter space, while the emulator bounds (i.e. the prior for each parameter, which we assume is uniform in each range) are reduced to increase the efficiency of drawing points that pass our distance threshold for computing the ABC posterior regions. We varied the parameters $\ln(\lambda_c)$ and $\ln(\lambda_p)$ separately in the optimization stage, while we trained and predicted on $\ln(\lambda_c \lambda_p)$ and $\ln(\lambda_p / \lambda_c)$ during the emulator stage (since these transformed parameters, the sum and difference of the log-rates of clusters and planets per cluster, appear more Gaussian).

Parameter	Clustered model (constant f_{swpa})			Clustered model (linear $f_{\text{swpa}}(b_p - r_p)$)		
	Optimizer bounds	λ_i	Emulator bounds	Optimizer bounds	λ_i	Emulator bounds
$f_{\sigma_{i,\text{high}}}$	(0, 1)	0.2	(0.1, 0.7)	(0, 1)	0.2	(0.1, 0.7)
$f_{\text{swpa,med}}^*$	(0, 1)	0.2	(0.3, 0.9)	(0, 1)	0.2	(0.3, 0.9)
$d_{f_{\text{swpa}}}/d(b_p - r_p)$	-	-	-	(-1, 1)	0.6	(0, 1)
$\ln(\lambda_c)$	($\ln(0.2)$, $\ln(10)$)	-	-	($\ln(0.2)$, $\ln(10)$)	-	-
$\ln(\lambda_p)$	($\ln(0.2)$, $\ln(10)$)	-	-	($\ln(0.2)$, $\ln(10)$)	-	-
$\ln(\lambda_c \lambda_p)$	-	1	(0, 3)	-	1	(0, 3)
$\ln(\frac{\lambda_p}{\lambda_c})$	-	2	(-2, 3)	-	2	(-2, 3)
α_P	(-2, 2)	1	(-0.8, 1.2)	(-2, 2)	1	(-0.8, 1.2)
α_{R1}	(-4, 2)	1	(-2.5, -0.5)	(-4, 2)	1	(-2.5, -0.5)
α_{R2}	(-6, 0)	1.5	(-6, -3)	(-6, 0)	1.5	(-6, -3)
σ_e	(0, 0.1)	0.02	(0, 0.04)	(0, 0.1)	0.02	(0, 0.04)
$\sigma_{i,\text{high}} (^\circ)$	(0, 90)	30	(0, 90)	(0, 90)	30	(0, 90)
$\sigma_{i,\text{low}} (^\circ)$	(0, $\sigma_{i,\text{high}}$)	1	(0, 2.4)	(0, $\sigma_{i,\text{high}}$)	1	(0, 2.4)
σ_R	(0, 0.5)	0.2	(0.1, 0.5)	(0, 0.5)	0.2	(0.1, 0.5)
σ_P	(0, 0.3)	0.1	(0.1, 0.3)	(0, 0.3)	0.1	(0.1, 0.3)

*This is just f_{swpa} for the clustered model with constant f_{swpa} .

2.3.1 Optimization stage

The first step in our procedure for model optimization involves passing the distance function given by equation 3 into a Differential Evolution optimizer², which implements a population-based genetic algorithm to minimize the target fitness function (i.e. our distance function). We run the optimizer for 5000 model evaluations, with $N_{\text{stars,sim}} = 79,935$ targets per evaluation, saving the results (model parameters and distances) at each iteration. Finally, we repeat the optimization process 50 times for each model and distance function (KS or AD) combination, each with a different starting point in the parameter space. The search bounds for the model parameters are listed in Table 2.

For each model and distance function, the optimization stage results in a pool of $5000 \times 50 = 2.5 \times 10^5$ model evaluations. We rank-order these sets of model parameters by their evaluated distance³, and keep every tenth point in the top 10^5 points so that we have a wide range of parameters (i.e. points both close to and far from the minima found by each run) for training the GP emulator.

2.3.2 GP emulator stage

The evaluations of the full forward model during the optimization stage are then used to train an emulator, which can “predict” the

outputs of the model (i.e. the distance function) given similar inputs (i.e. model parameters). For our emulator, we use a Gaussian process (GP) model (Rasmussen & Williams 2006) that is described by a prior mean function $m(\mathbf{x})$ and a covariance (i.e. kernel) function $k(\mathbf{x}, \mathbf{x}'; \phi)$:

$$f(\mathbf{x}) \sim \mathcal{GP}(m(\mathbf{x}), k(\mathbf{x}, \mathbf{x}'; \phi)), \quad (4)$$

$$k(\mathbf{x}, \mathbf{x}'; \phi) = \sigma_f^2 \exp \left[-\frac{1}{2} \sum_i \frac{(x_i - x_i')^2}{\lambda_i^2} \right], \quad (5)$$

where $f(\mathbf{x}) = \mathcal{D}_W$ is the distance function we wish to model, \mathbf{x} (and \mathbf{x}') are the model parameters, and $\phi = (\sigma_f, \lambda_1, \lambda_2, \dots, \lambda_d)$ are the hyperparameters of the kernel. The values of the hyperparameters are also listed in Table 2. In particular, σ_f determines the strength of correlation between points and also acts as the standard deviation of the Gaussian prior (i.e., for points far away from any training data, the emulator effectively returns draws from a Gaussian distribution with mean $m(\mathbf{x})$ and standard deviation σ_f), while λ_i are the length scales in each dimension over which points are correlated.

We choose a constant prior mean function, with a value that is set towards the higher end of the distances of the training points. In this way, emulated distances at points far away from any training points will be significantly worse than the best distances achievable by our model, while emulated distances will only be lower than the mean function if they are near training points and these points suggest that the model is good in the vicinity. In practice, we also find that the AD distance is significantly more sensitive to deviations from a perfect model than the KS distance; we thus set $m(\mathbf{x}) = 75$ for the distance function involving KS distances, and $m(\mathbf{x}) = 150$ for the distance function involving AD distances. We verify that our results do not change much with differing choices for the mean function, as long as it is well above the minimum distances found by the optimizer and the distance threshold for constructing the ABC posterior.

² We use the “BlackBoxOptim” package (<https://github.com/robertfeldt/BlackBoxOptim.jl>), which provides several algorithms for general optimization problems. We choose the “adaptive_de_rand_1_bin_radiuslimited” optimizer and set the population size to four times the number of free model parameters.

³ After ranking, we re-evaluate the distances at each of these points by regenerating a new simulated catalogue, in order to avoid the bias that would result in keeping smaller-than-average distances at these points due to the combination of the stochastic nature of our simulations and the mere process of ranking.

2.3.3 ABC for model inference

In order to compute the credible regions for the model parameters, we construct an ABC posterior distribution by using the emulator to predict the model at a large number of points and accept those that pass a distance threshold. These points are drawn from the prior, for which we assume a uniform distribution in the d -dimensional box (with bounds based on inspection of the training points, as listed in Table 2). In this paper, our distance function given by equation 3 (KS or AD) includes 27 individual distance terms, weighted and summed such that even a perfect model results in a distance of $\sim 27 \pm 2.7$. We choose distance thresholds of $\mathcal{D}_{W,KS} = 40$ and $\mathcal{D}_{W,AD} = 70$ for our linear $f_{\text{swpa}}(b_p - r_p)$ model (and slightly larger thresholds, $\mathcal{D}_{W,KS} = 45$ and $\mathcal{D}_{W,AD} = 75$, for our constant f_{swpa} model, since this is a worse model as we will show in §3). These thresholds are close to (slightly larger than) the best distances found during the optimization stage, and result in an efficiency of roughly 10^{-5} for the fraction of drawn points accepted (drawn uniformly in our box). We collect 5×10^4 points with emulated distances passing the distance threshold to serve as the ABC posterior for the model parameters. For more detailed calculations, we also simulate the full forward model and require that both the emulated and true distances pass the distance threshold.

3 RESULTS

In this section, we first report and discuss the main results, beginning with a comparison to the clustered periods and sizes model in Paper I, before describing our findings for the model stellar dependence. In Table 3, we list the best-fitting values and 68.3% credible regions for the free parameters of both the clustered model with constant f_{swpa} and the clustered model with linear $f_{\text{swpa}}(b_p - r_p)$. We show the same credible regions (i.e. ABC posterior distributions) from our KS analysis in Figure 2 for the linear $f_{\text{swpa}}(b_p - r_p)$ model and in supplemental Figure A1 for our constant f_{swpa} model.

3.1 The overall fraction of stars with planets

The only difference between our baseline model (constant f_{swpa}) and the clustered periods and sizes model in Paper I is a re-parametrization from a Poisson to a zero-truncated Poisson distribution for the number of clusters per system with the addition of an explicit parameter f_{swpa} for the fraction of stars with planets. As explained in §2.1.1, this change was made to 1) decouple the number of intrinsic zero-planet systems from the planet-hosting stars and their underlying multiplicity distribution and 2) produce a baseline model for comparison to our more general, linear $f_{\text{swpa}}(b_p - r_p)$ model. Methodologically, we also used a distance function with three times the number of terms (fitting to the bluer half, redder half, and full samples) and recomputed weights, in order to facilitate a direct comparison with our new model. We first discuss how these results compare with the results from Paper I.

The fraction of stars with planets: For our baseline model, we find that the fraction of stars with planets (in our entire range explored, with periods between 3 and 300 d and planet radii between 0.5 and $10R_{\oplus}$) is well constrained. The KS analysis results in $f_{\text{swpa}} = 0.61^{+0.12}_{-0.13}$, while the AD analysis gives a somewhat lower value of $f_{\text{swpa}} = 0.46^{+0.20}_{-0.09}$ although the 68.3% credible regions overlap. These credible regions are also consistent with the results from the clustered periods and sizes model in Paper I, where the fraction of stars with planets in the same range is $0.56^{+0.18}_{-0.15}$ (via the KS

analysis). This is noteworthy, given that we find a meaningful and comparable constraint on the f_{swpa} despite a re-parametrization of the intrinsic multiplicity distribution and the extra dimensionality of the model optimization problem (and thus a larger parameter space).

The distribution of planets between and within clusters: While our baseline model and the clustered models from Paper I all have a parameter λ_c (for the mean rate of attempted clusters per planetary system), this parameter is not the same in these models. In Paper I, λ_c is the mean number of clusters per system before any rejection sampling, and due to the draws from a Poisson distribution, is also tied to the number of true zero-planet systems. Loosely, it could be interpreted as the mean number of clusters per star, including those that harbour no planets (between 3 and 300 d), although we found that the true mean is somewhat lower than what the parameter value suggests due to the rejected clusters. For our clustered periods and sizes model, about $\sim 79\%$ and $\sim 19\%$ of planet-hosting stars have just one and two clusters, respectively (Figure 1). Since the fraction of stars with planets in that model is $\sim 56\%$, this means that the true mean number of clusters per system is about $\sum_{n_c \geq 0} (f_c n_c) \sim 0.7$, where f_c is the fraction of all stars with n_c clusters, while the mean number of clusters per system with planets is $\sum_{n_c \geq 1} (f_c / 0.56) n_c \sim 1.2$.

In this paper, we have decoupled the λ_c parameter from the number of zero-planet systems and thus the fraction of stars with planets. However, we find that the mean numbers of clusters (and planets per cluster) are rather poorly constrained. For our constant f_{swpa} model, we find that the mean rate of clusters per system is $1.46^{+1.96}_{-0.82}$ ($4.06^{+1.81}_{-2.09}$) using KS (AD) analyses. While there is a great difference between our KS and AD results, the uncertainties are also large and overlap. Part of the reason we find such a large range of λ_c values is due to our algorithm for drawing planetary systems – as in Paper I, we draw clusters one by one, drawing their period scales after the unscaled periods for each planet in a cluster have been drawn, and only keeping clusters that can fit.⁴ As such, the actual number of accepted clusters can be significantly less than what would be suggested by the value of the λ_c parameter. Thus, we warn that our parameter values of λ_c (and λ_p) should not be misinterpreted as the average number of clusters per system (or average number of planets per cluster). Instead, we count the true numbers of clusters and planets per cluster, as shown in Figure 1 for the KS analysis. The AD analysis (not shown) leads to more clusters per system and fewer planets per cluster, but a similar intrinsic planet multiplicity distribution (i.e. the top panel). We conclude that our decoupling of the λ_c parameter suggests that the true mean number of clusters per system is greater than what we found in Paper I, but the extent is unclear and is degenerate with the mean number of planets per cluster.

As noted earlier in §2.1.1, it is interesting that our re-parametrization of the intrinsic multiplicity distribution did not change the inferred distribution of total planet multiplicity in any noticeable way (i.e. compared to the red dotted line in the top panel of Figure 1). We also note that our intrinsic planet multiplicity distribution is very different than of that inferred by Sandford, Kipping, & Collins (2019), who found that a single Zipfian distribution (a discrete power-law distribution) which peaks at unity and falls off

⁴ In this manner, each individual cluster is deemed “stable” (given our minimum spacing in mutual Hill radii for adjacent planet pairs) before their period scale has been drawn, but the period scale drawn must also allow all the planets in the cluster to be stable with the previously drawn clusters.

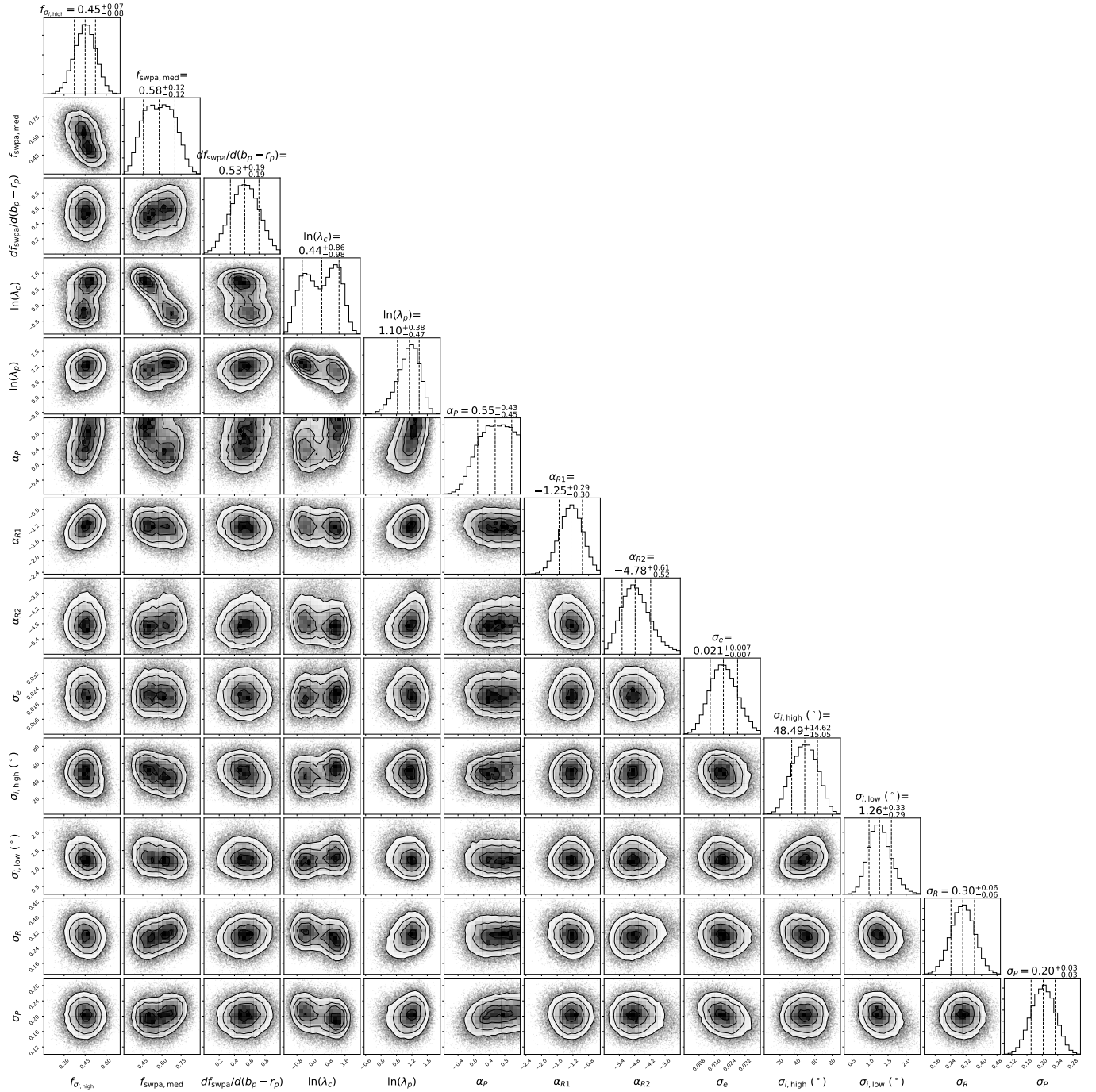


Figure 2. The ABC posterior distributions of the free model parameters of the clustered model with linear $f_{\text{swpa}}(b_p - r_p)$. A total of 5×10^4 points passing a distance threshold of $\mathcal{D}_{W, \text{KS}} = 40$ as drawn from the GP emulator are shown. The prior mean function was set to a constant value of 75.

rapidly towards larger multiplicities best fits the observed *Kepler* counts. In contrast, our distribution peaks at a count of ~ 4 planets (for planet hosting stars), with a similar fraction of 7-planet systems as 1-planet systems. However, [Sandford, Kipping, & Collins \(2019\)](#) did not fit the rate of zero-planet systems (i.e. the fraction of stars with planets). These results highlight the importance of modelling the true fraction of stars with planets and simultaneously fitting the additional observables (period ratio distribution, etc. as we have done here) when inferring the underlying multiplicity distribution,

in order to distinguish between competing models for the *Kepler* dichotomy.

3.2 Planetary system architectures

Broadly, we find consistent results for the model parameters describing the planetary system architectures between our new models and our old clustered periods and sizes model. We summarize the results here, quoting the KS results for our baseline model. The results for

Table 3. Best-fitting values for the free parameters of each model. While we trained the emulator on the transformed parameters $\ln(\lambda_c \lambda_p)$ and $\ln(\lambda_p / \lambda_c)$, we transform back to $\ln(\lambda_c)$ and $\ln(\lambda_p)$ for reporting the credible intervals. Unlogged rates λ_c and λ_p are shown for interpretability, and are equivalent to the rows with log-values. The 68.3% credible regions are computed from the ABC posterior using distance thresholds of $\mathcal{D}_{W,KS} = 45$ and $\mathcal{D}_{W,KS} = 40$ for the constant f_{swpa} and linear $f_{\text{swpa}}(b_p - r_p)$ models, respectively, in the KS analyses, while the distance thresholds are $\mathcal{D}_{W,AD} = 75$ and $\mathcal{D}_{W,AD} = 70$, respectively, in the AD analyses.

Parameter	Clustered periods and sizes model from Paper I			Clustered model (constant f_{swpa})		Clustered model (linear $f_{\text{swpa}}(b_p - r_p)$)		
	Ref. catalogue	Best-fit KS	Best-fit AD	Best-fit KS	Best-fit AD	Figure 6	Best-fit KS	Best-fit AD
$f_{\sigma_{i,\text{high}}}$	0.4	$0.42^{+0.08}_{-0.07}$	$0.40^{+0.11}_{-0.12}$	$0.42^{+0.09}_{-0.08}$	$0.50^{+0.10}_{-0.10}$	0.45	$0.45^{+0.07}_{-0.08}$	$0.47^{+0.10}_{-0.10}$
$f_{\text{swpa,med}}^*$	-	-	-	$0.61^{+0.12}_{-0.13}$	$0.46^{+0.20}_{-0.09}$	0.6	$0.58^{+0.12}_{-0.12}$	$0.56^{+0.13}_{-0.11}$
$df_{\text{swpa}}/d(b_p - r_p)$	-	-	-	-	-	0.6	$0.53^{+0.19}_{-0.19}$	$0.62^{+0.17}_{-0.19}$
$\ln(\lambda_c)$	-0.22**	$-0.10^{+0.44}_{-0.35}$ **	$0.24^{+0.33}_{-0.40}$ **	$0.38^{+0.85}_{-0.83}$	$1.40^{+0.37}_{-0.72}$	0.69	$0.44^{+0.86}_{-0.98}$	$0.99^{+0.64}_{-0.85}$
λ_c	0.8^{**}	$0.90^{+0.50}_{-0.26}$ **	$1.27^{+0.50}_{-0.42}$ **	$1.46^{+1.96}_{-0.82}$	$4.06^{+1.81}_{-2.09}$	2.0	$1.55^{+2.12}_{-0.97}$	$2.69^{+2.41}_{-1.54}$
$\ln(\lambda_p)$	1.31	$1.35^{+0.36}_{-0.44}$	$0.73^{+0.60}_{-0.56}$	$0.88^{+0.41}_{-0.51}$	$0.29^{+0.53}_{-0.42}$	0.92	$1.10^{+0.38}_{-0.47}$	$0.68^{+0.46}_{-0.46}$
λ_p	3.7	$3.86^{+1.67}_{-1.38}$	$2.08^{+1.70}_{-0.89}$	$2.41^{+1.22}_{-0.96}$	$1.34^{+0.93}_{-0.46}$	2.5	$3.00^{+1.39}_{-1.13}$	$1.97^{+1.15}_{-0.73}$
α_P	0.4	$0.40^{+0.64}_{-0.56}$	$0.07^{+0.66}_{-0.45}$	$0.40^{+0.45}_{-0.43}$	$0.43^{+0.42}_{-0.36}$	0.6	$0.55^{+0.43}_{-0.45}$	$0.65^{+0.37}_{-0.44}$
α_{R1}	-1.0	$-1.02^{+0.64}_{-0.70}$	$-1.27^{+0.26}_{-0.25}$	$-1.29^{+0.33}_{-0.33}$	$-1.37^{+0.22}_{-0.22}$	-1.4	$-1.25^{+0.29}_{-0.30}$	$-1.45^{+0.24}_{-0.24}$
α_{R2}	-4.4	$-4.41^{+1.36}_{-0.79}$	$-5.08^{+0.71}_{-0.54}$	$-4.80^{+0.66}_{-0.55}$	$-5.01^{+0.55}_{-0.47}$	-4.8	$-4.78^{+0.61}_{-0.52}$	$-4.91^{+0.54}_{-0.50}$
σ_e	0.020	$0.020^{+0.014}_{-0.010}$	$0.014^{+0.010}_{-0.008}$	$0.020^{+0.009}_{-0.008}$	$0.016^{+0.006}_{-0.006}$	0.019	$0.021^{+0.007}_{-0.007}$	$0.016^{+0.007}_{-0.006}$
$\sigma_{i,\text{high}} (^{\circ})$	50	48^{+17}_{-17}	49^{+23}_{-25}	44^{+18}_{-16}	45^{+18}_{-17}	45	48^{+15}_{-15}	37^{+20}_{-15}
$\sigma_{i,\text{low}} (^{\circ})$	1.4	$1.40^{+0.54}_{-0.39}$	$1.29^{+0.35}_{-0.32}$	$1.26^{+0.34}_{-0.30}$	$1.24^{+0.26}_{-0.25}$	1.25	$1.26^{+0.33}_{-0.29}$	$1.23^{+0.30}_{-0.28}$
σ_R	0.3	$0.31^{+0.07}_{-0.07}$	$0.32^{+0.07}_{-0.07}$	$0.30^{+0.06}_{-0.07}$	$0.27^{+0.07}_{-0.07}$	0.3	$0.30^{+0.06}_{-0.06}$	$0.32^{+0.06}_{-0.07}$
σ_P	0.2	$0.21^{+0.04}_{-0.04}$	$0.20^{+0.04}_{-0.04}$	$0.20^{+0.03}_{-0.03}$	$0.19^{+0.03}_{-0.03}$	0.2	$0.20^{+0.03}_{-0.03}$	$0.19^{+0.03}_{-0.03}$

*This is just f_{swpa} for the clustered model with constant f_{swpa} .

**Although the symbol for this parameter is the same, the parameter is not: in Paper I, a Poisson distribution for the number of clusters is used, while in this paper, a zero-truncated Poisson distribution is used. Thus, λ_c can be interpreted as the mean number of attempted clusters per system in Paper I, and as the mean number of attempted clusters per system with planets in this paper. In both cases some clusters are rejected due to stability.

our linear $f_{\text{swpa}}(b_p - r_p)$ model, and AD results, are listed in Table 3 and very similar. For a more detailed discussion of what these parameters mean and comparisons to other values in the literature, see §3 of Paper I.

Period distribution (α_P): the overall period distribution is described by a single power-law between 3 and 300 d, with a shallowly increasing occurrence in log period given by $\alpha_P = 0.40^{+0.45}_{-0.43}$.

Radius distribution (α_{R1}, α_{R2}): the overall radius distribution is described by a broken power-law between 0.5 and $10R_{\oplus}$, where we have set the break at $R_{p,\text{break}} = 3R_{\oplus}$. For planets below the break, the distribution is consistent with flat, $\alpha_{R1} = -1.29^{+0.33}_{-0.33}$, above, there is a sharp fall-off with $\alpha_{R2} = -4.80^{+0.66}_{-0.55}$. As before, our models do not have the flexibility of producing a radius valley.

Eccentricity distribution (σ_e): we find small orbital eccentricities, described by a Rayleigh scale $\sigma_e = 0.020^{+0.009}_{-0.008}$. While our models reproduce the transit duration and period-normalized transit duration ratio (ξ) distributions reasonably well, there may be evidence for a higher eccentricity component based on comparisons to the circular-normalized transit duration distribution ($t_{\text{dur}}/t_{\text{circ}}$, where $t_{\text{circ}} = \frac{R_* P}{\pi a}$ is the duration assuming a circular orbit with impact parameter $b = 0$), although we have not included this distribution in our distance function.

Mutual inclination distribution ($f_{\sigma_{i,\text{high}}}, \sigma_{i,\text{high}}, \sigma_{i,\text{low}}$): we still find clear evidence for a dichotomous population of planetary systems in terms of their mutual inclinations, with $f_{\sigma_{i,\text{high}}} =$

$0.42^{+0.09}_{-0.08}$ of systems assigned to the high mutual inclination population. As in our models from Paper I (except where noted), in our new models we still draw mutual inclinations from $\sigma_{i,\text{low}}$ for planets near an MMR with another planet, which affects about $\approx 30\%$ of all planets. The high mutual inclination scale $\sigma_{i,\text{high}}$, while clearly and significantly greater than $\sigma_{i,\text{low}}$, is still largely unconstrained at larger values since these systems primarily affect only the observed number of single-transiting systems, and our simple stability criteria does not directly account for the mutual inclinations. The low mutual inclination scale, $\sigma_{i,\text{low}} = 1.26^{+0.34}_{-0.30}$ degrees, suggests that most multi-planet systems are near but not exactly coplanar.

Period and radius clustering (σ_P, σ_R): the periods and planet radii of planets in the same cluster are each highly correlated. We find that $\sigma_P = 0.20 \pm 0.03$, where this parameter quantifies the width per planet in the cluster for each cluster, in log-period. On the other hand, $\sigma_R = 0.30^{+0.06}_{-0.07}$, which is the cluster scale in log-radius (regardless of the number of planets in the cluster). These two parameters are most directly constrained by the period ratio and transit depth (i.e radius) ratio distributions, respectively.

3.3 The occurrence of planetary systems with spectral type

We find a significant positive slope for the linear relation between f_{swpa} and the $b_p - r_p$ color, suggesting that the occurrence rate of planetary systems between 3 and 300 d increases towards later

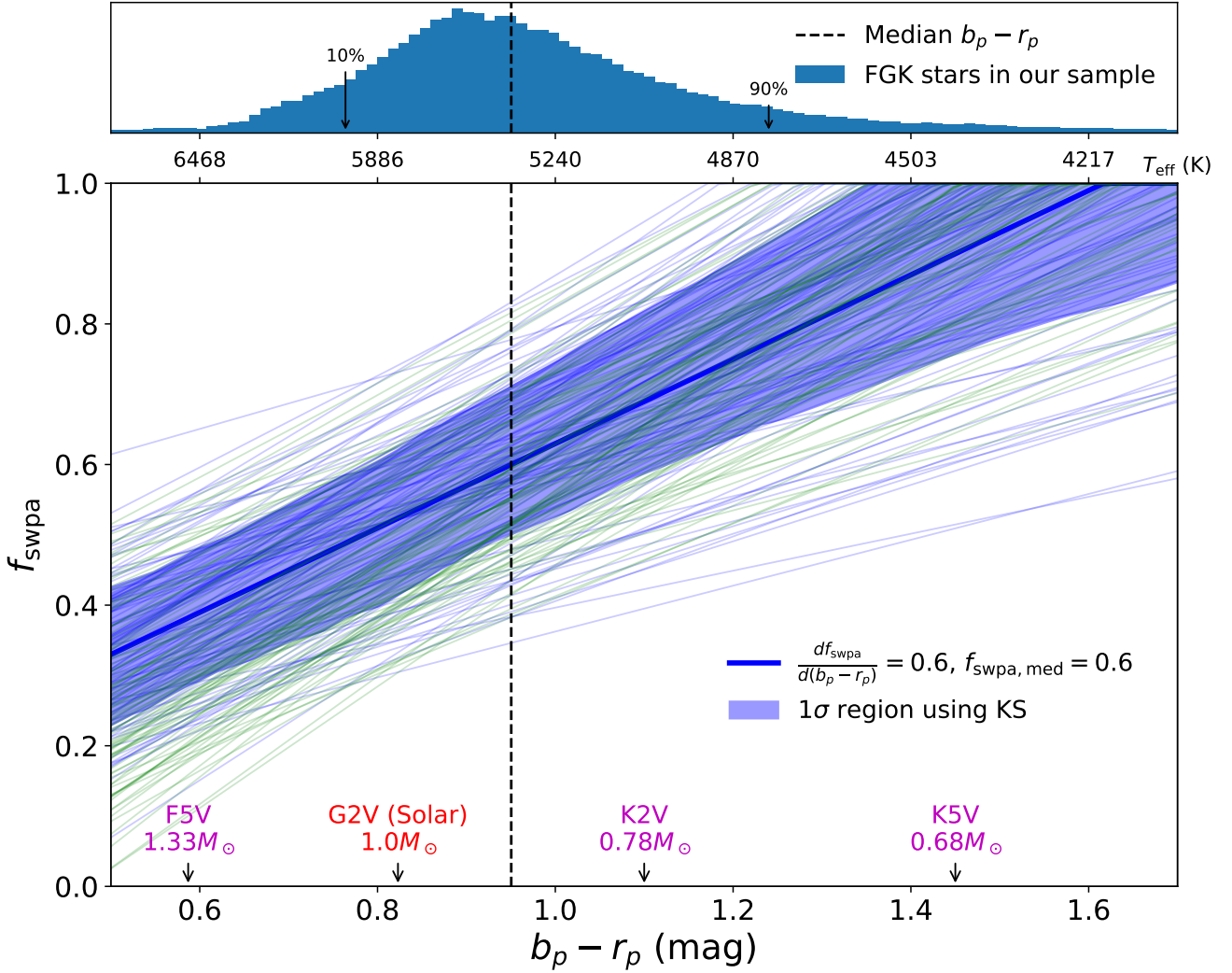


Figure 3. The best-fitting relation for the fraction of stars with planets f_{swpa} as a function of the *Gaia* $b_p - r_p$ colour, from our linear model. Light blue and green lines show 100 best models each passing our KS and AD distance thresholds, respectively. The bolded blue line shows a single model with $df_{\text{swpa}}/d(b_p - r_p) = 0.6$ and $f_{\text{swpa,med}} = 0.6$ (i.e., the same values used to generate the catalogue in Figure 6), while the shaded blue region represents the 68.3% credible interval from our KS analysis. The dashed vertical line denotes the median colour of our sample ($(b_p - r_p)_{\text{med}} \approx 0.95$). A few other exemplary values (magenta) are labeled with arrows, including red for the solar value ($T_{\text{eff}} = 5770$ K), where we have used a table relating T_{eff} and $b_p - r_p$ from [Pecaut & Mamajek \(2013\)](#). The fraction of Sun-like stars with planets (with orbital periods in the range 3–300 d and radii in the range $0.5 - 10R_{\oplus}$) is very close to half. The fraction increases by over a factor of two from the bluest (early F) to the reddest (late K) dwarfs in our sample, and reaches 100% at $b_p - r_p \approx 1.6$, which may suggest that a more complicated model than a linear relation is necessary. The top panel shows a histogram for the distribution of $b_p - r_p$ colours for our stellar sample, where arrows indicate the 10% and 90% quantiles.

type (redder, increasing $b_p - r_p$) stars. The slope is $df_{\text{swpa}}/d(b_p - r_p) = 0.53^{+0.19}_{-0.19}$ ($0.62^{+0.17}_{-0.19}$) using KS (AD) analyses. Both analyses result in a similar slope and strongly disfavour a flat or negative slope. As expected, the fraction of stars with planets at the median color ($f_{\text{swpa,med}}$), is comparable to the overall fraction of stars with planets (i.e. f_{swpa}) for our baseline model; we find that $f_{\text{swpa,med}} = 0.58^{+0.12}_{-0.12}$ ($0.56^{+0.13}_{-0.11}$) using KS (AD) analyses.

In Figure 3, we plot our best-fitting relation for the linear $f_{\text{swpa}}(b_p - r_p)$ model. The solid blue line shows an exemplary line that is close to the median relation, with $df_{\text{swpa}}/d(b_p - r_p) = 0.6$ and $f_{\text{swpa,med}} = 0.6$. We also plot 100 individual models passing each of our KS and AD distance thresholds, as light blue and green lines respectively, and denote the 68.3% credible region from the KS

analysis by the shaded blue region. The vertical dashed line denotes the median $b_p - r_p$ color of our stellar sample, whose distribution of $b_p - r_p$ is plotted as a histogram in the top panel. We use the table from [Pecaut & Mamajek \(2013\)](#) to adopt a relation between *Gaia* $b_p - r_p$ color and stellar effective temperature T_{eff} , which we label as a secondary x-axis in Figure 3.

Given that our stellar sample ranges from $b_p - r_p \approx 0.5$ to ≈ 1.7 , the large slope for our linear relation suggests that the fraction of stars with planets changes by over a factor of two going from the bluest stars (early F dwarfs) to the reddest stars (late K dwarfs) in our sample. For F2V dwarfs, $f_{\text{swpa}}(0.5) = 0.34^{+0.08}_{-0.11}$, while this value increases to $f_{\text{swpa}}(1.4) = 0.91^{+0.09}_{-0.18}$ for mid K dwarfs. The f_{swpa} rises to unity at $b_p - r_p \approx 1.6$ ($T_{\text{eff}} \approx 4200$ K), implying

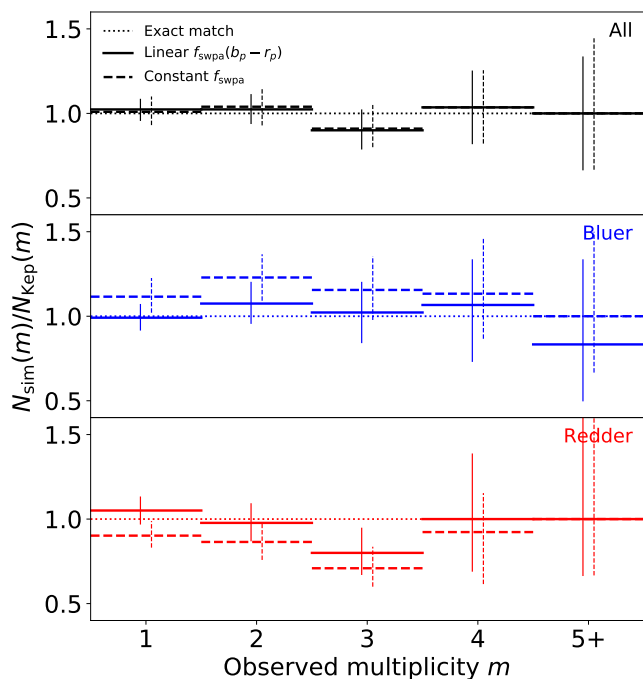


Figure 4. The observed multiplicity distributions of our models, normalized by the *Kepler* multiplicity distribution. The panels from top to bottom include the full sample (“All”) and the bluer and redder halves (respectively labeled and coloured). In each panel, the solid and dashed lines represent the median multiplicities (normalized to the *Kepler* counts) for our linear $f_{\text{swpa}}(b_p - r_p)$ and constant f_{swpa} models, respectively. Vertical lines denote the 68.3% credible regions. The multiplicity counts used to generate this figure are also listed in Table 4, and result from our KS analysis. We show a dotted horizontal line at $N_{\text{sim}}(m)/N_{\text{Kep}}(m) = 1$ as a reference for exact matches to the *Kepler* data. While both models fit the overall multiplicity distribution equally well (top panel), the constant f_{swpa} model overproduces observed systems around the bluer stars and underproduces systems around the redder stars in our sample. Our linear $f_{\text{swpa}}(b_p - r_p)$ model is a much better fit to the observed multiplicities for these two subsets.

that inner planetary systems are extremely common around cooler stars. A more complex model than a simple linear relation may be necessary to model differences at this range of stellar types. We also note that while we assume a linear relation, we fit it using two samples split at the median stellar colour, around which most of our stars are concentrated. Finally, the fraction of solar-type (G2V) dwarfs harbouring at least one planet between 3 and 300 d is $f_{\text{swpa}} = 0.54^{+0.08}_{-0.13}$, or roughly half.

4 DISCUSSION

4.1 The observed multiplicity distribution

In Table 4, we list the observed multiplicity counts from the *Kepler* data and our models (constant f_{swpa} and linear $f_{\text{swpa}}(b_p - r_p)$), in both the total (“All”) sample as well as in the bluer and redder halves. For the multiplicity counts observed from our models, we also compute and list uncertainties from generating 1000 simulated catalogues that pass our (KS) distance threshold. The results using our AD distance threshold are similar for the median values but provide somewhat larger uncertainties (which we have not listed here). We note that the 68.3% credible regions we computed include

two sources of uncertainty: 1) the Monte Carlo noise due to the finite number of targets used for each simulated catalogue (which we set to be equal to the number of targets in our *Kepler* stellar sample, 79,935 stars), and 2) the differences in the models due to the uncertainties in the model parameters, for which we only keep sets of parameters passing the distance threshold after one realization of a simulated catalogue.

To facilitate a more direct comparison between the multiplicity distributions observed in the *Kepler* catalogue and our models, we also plot the ratios of our models to the *Kepler* counts, $N_{\text{sim}}(m)/N_{\text{Kep}}(m)$, for each observed planet multiplicity order m in Figure 4. We show panels for the total, bluer, and redder samples, computing the ratios of observed model counts to *Kepler* counts for each sample. In each panel, horizontal bars denote the ratio values (an exact match is given by a ratio of 1, guided by the dotted line), while vertical lines show the 68.3% credible intervals (as listed in Table 4). The dashed and solid lines plot the results from our constant f_{swpa} and linear $f_{\text{swpa}}(b_p - r_p)$ models, respectively. Systems with $m \geq 5$ observed planets are binned together here due to their low counts (the same multiplicity binning is also done in our distance function, when computing D_{mult} in equation 3).

Both models fit the overall multiplicity distribution equally well. This is expected, as Paper I showed that a clustered model (with two populations of mutual inclinations) is necessary and fits the observed multiplicity distribution extremely well; both models in this paper are extensions of that model. For almost all multiplicity orders m , the median observed counts from our models very closely matches the *Kepler* count, and the latter falls within our 68.3% credible intervals. The biggest difference is the number of triples ($m = 3$), as more triple systems are observed in the data (100, given our period-radius range and stellar sample) than what our models produce. However, the value predicted is still within the 68.3% credible intervals (91^{+14}_{-11} and 90^{+12}_{-11} for our constant and linear f_{swpa} models, respectively).

The need for a stellar-dependent f_{swpa} is clear when considering the bluer and redder halves of our FGK dwarf sample. Our baseline (constant f_{swpa}) model consistently overproduces the rate of observed planetary systems around bluer stars and underproduces the rate around redder stars. This trend is significant at all observed multiplicity orders except the higher ones at $m = 4$ and $m \geq 5$, where the relatively low counts reduce the statistical power to distinguish between the two models. On the other hand, our linear $f_{\text{swpa}}(b_p - r_p)$ model provides a significantly better match to the observed multiplicity distributions around both the bluer and redder halves. Interestingly, while the number of observed triples is a near exact match in the bluer sample, there is a higher occurrence of triples in the redder sample than what our model produces. Nevertheless, the excellent similarity between the multiplicity distributions of this model and the *Kepler* data for both bluer and redder halves is remarkable, given that our model assumes a very simple stellar dependence: the fraction of stars with planets as a simple linear function of the Gaia $b_p - r_p$ color, and that we have *not* made any other parameters of the model depend on the stellar properties. In particular, the intrinsic multiplicity distribution (i.e. parametrization using zero-truncated Poisson distributions with λ_c and λ_p for the number of clusters and planets per cluster, respectively) remains the same for both models, aside from a difference in the fraction of stars for which we draw planetary systems.

Table 4. A comparison of the observed multiplicity distribution between the *Kepler* data and our models, counting all stars (79,935) and the bluer and redder halves in our sample (respectively named). The “Bluer” and “Redder” columns add up to the “All” columns. For each model, the 68.3% credible intervals are computed from 1000 simulated catalogues passing the (KS) distance threshold (the results from our AD analyses, not shown, are similar but yield somewhat larger uncertainties). While both the constant f_{swpa} and the linear $f_{\text{swpa}}(b_p - r_p)$ models fit the overall (“All”) multiplicity distribution equally well (and produce nearly identical distributions), the linear model produces a much better match to the observed multiplicities of both the bluer and redder halves.

Observed multiplicity m	<i>Kepler</i> data			Clustered model (constant f_{swpa})			Clustered model (linear $f_{\text{swpa}}(b_p - r_p)$)		
	All	Bluer	Redder	All	Bluer	Redder	All	Bluer	Redder
1 (singles)	1171	579	592	1182^{+106}_{-92}	646^{+64}_{-55}	534^{+51}_{-42}	1198^{+70}_{-76}	574^{+45}_{-42}	622^{+47}_{-47}
2 (doubles)	253	120	133	263^{+28}_{-28}	148^{+16}_{-16}	115^{+15}_{-14}	259^{+22}_{-21}	129^{+15}_{-14}	130^{+15}_{-14}
3 (triples)	100	45	55	91^{+14}_{-11}	52^{+9}_{-8}	39^{+7}_{-6}	90^{+12}_{-11}	46^{+8}_{-8}	44^{+8}_{-7}
4 (quadruples)	28	15	13	29^{+6}_{-6}	17^{+5}_{-4}	12^{+3}_{-4}	29^{+6}_{-6}	16^{+4}_{-5}	13^{+5}_{-4}
5 (quintuples)	6	4	2	7^{+4}_{-2}	5^{+2}_{-2}	3^{+2}_{-2}	7^{+3}_{-3}	4^{+2}_{-2}	3^{+2}_{-2}
6 (sextuples)	3	2	1	1^{+2}_{-1}	1^{+1}_{-1}	0^{+1}_{-0}	1^{+2}_{-1}	1^{+1}_{-1}	0^{+1}_{-0}
7 (septuples)	0	0	0	0^{+1}_{-0}	0^{+1}_{-0}	0^{+0}_{-0}	0^{+1}_{-0}	0^{+0}_{-0}	0^{+0}_{-0}
8 (octuples)	0	0	0	0^{+0}_{-0}	0^{+0}_{-0}	0^{+0}_{-0}	0^{+0}_{-0}	0^{+0}_{-0}	0^{+0}_{-0}
Total planets: $\sum mN(m)$	2137	1046	1091	2146^{+176}_{-145}	1201^{+103}_{-92}	943^{+86}_{-66}	2146^{+109}_{-101}	1062^{+68}_{-72}	1085^{+72}_{-64}

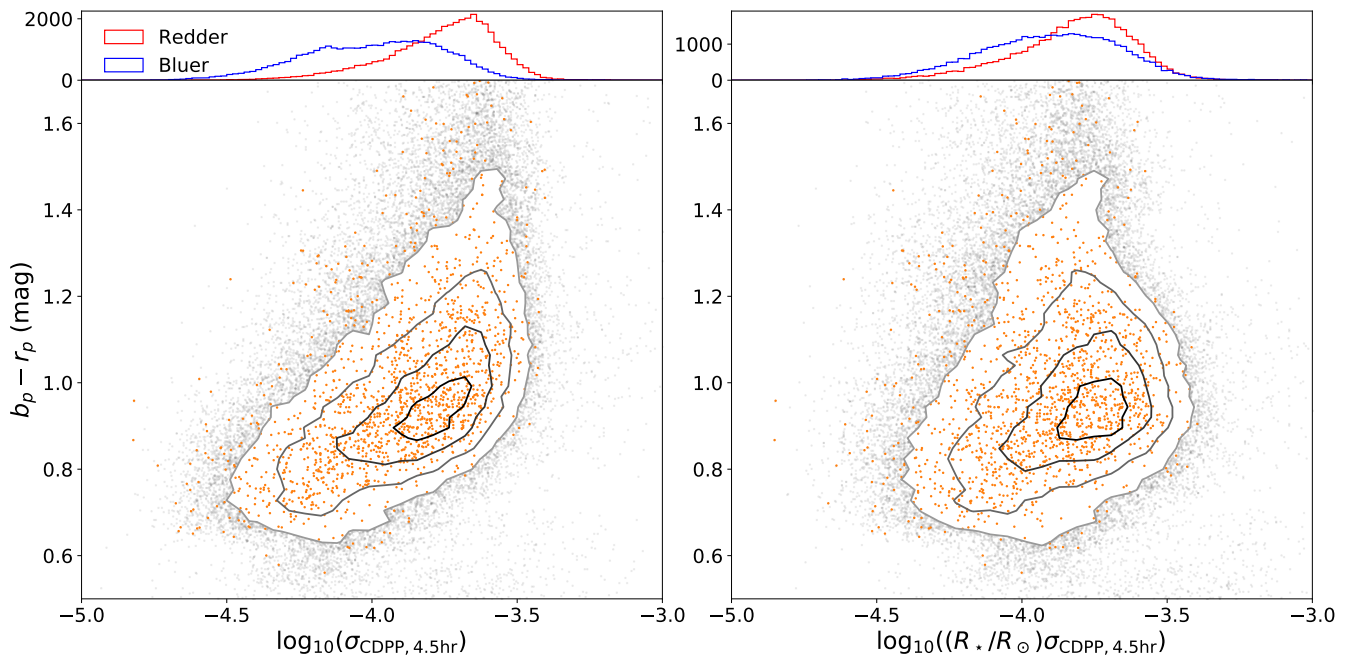


Figure 5. **Left-hand side:** scatter plot of $\sigma_{\text{CDPP},4.5\text{hr}}$ vs. $b_p - r_p$ for our sample of FGK stars. The grey points denote all 79,935 target stars in our sample, where four contour levels enclosing 11.8%, 39.3%, 67.5%, and 86.5% of the points (from innermost to outermost levels) are plotted. The orange points denote the stars hosting planet candidates (between $0.5 - 10R_{\oplus}$ and 3 – 300 d). The top panel shows histograms of $\sigma_{\text{CDPP},4.5\text{hr}}$ for all target stars (i.e. grey points) in our bluer and redder halves, as respectively coloured and labeled. **Right-hand side:** same as the left-hand panels, but using $R_*\sigma_{\text{CDPP},4.5\text{hr}}$ for the x-axis, rather than $\sigma_{\text{CDPP},4.5\text{hr}}$. The distribution of $R_*\sigma_{\text{CDPP},4.5\text{hr}}$ for our blue sample is shifted to slightly smaller values (i.e. lower limit of detectability) than that of our red sample. Thus, while the larger radii of the bluer stars penalizes the detectability of transiting planets, their lower CDPP values more than offsets this bias, making it slightly easier to detect planets of a given size around them.

4.2 Why is it easier to detect planets around hotter stars?

On first glance, it appears that the numbers of planets may be constant across all FGK dwarf stars. As we show in Table 4, splitting our *Kepler* sample of stars into two halves based on their Gaia $b_p - r_p$ colors also roughly divides the observed numbers of planets almost

equally. There are slightly more planets in the redder half than in the bluer half at low multiplicity orders ($m \leq 3$) and a reversal at $m \geq 4$, although there are fewer systems at higher multiplicities and the differences are very small. However, in this paper we showed with our forward model that we get a significantly higher rate of

observed planets around stars in the bluer half than the redder half if we assume the same distribution of planetary systems (i.e. our baseline, constant f_{swpa} model). Indeed, this is why we require a dependence on the stellar color/effective temperature that rises towards cooler, redder stars for the occurrence of planetary systems in order to produce similar numbers of observed planets in both stellar samples. So why is it easier to detect planets of a given size and period around hotter stars?

On one hand, the larger sizes of bluer (hotter) stars provides one clear disadvantage for detecting transiting planets of a given size, since to first order the transit depth is given by the fraction of the stellar disc area blocked by the planet, $\delta \simeq (R_p/R_\star)^2$, i.e. it is inversely proportional to the stellar radius squared. On the other hand, planets are more likely to transit larger stars simply due to the increased geometric transit probability ($\sim R_\star/a$). Larger stars may also induce longer transit durations due to the distance a planet must travel in order to cross the stellar disc. However, we find that the biggest factor contributing to the increased detection efficiency of planets around bluer stars in the *Kepler* mission is their improved photometric precision over that of redder stars. To illustrate this effect, we plot the root-mean-square Combined Differential Photometric Precision (Christiansen et al. 2012), σ_{CDPP} (4.5 hr duration for simplicity). The left-hand panel of Figure 5 shows a scatter plot of $(\log) \sigma_{\text{CDPP},4.5\text{hr}}$ vs. $b_p - r_p$, for all the stars (grey points) and planet-hosting stars (orange points) in our sample. Similarly, the right-hand panel of Figure 5 shows a scatter plot of $(\log) R_\star \sigma_{\text{CDPP},4.5\text{hr}}$ vs. $b_p - r_p$. To avoid overcrowding in Figure 5, we plot contours enclosing 11.8%, 39.3%, 67.5%, and 86.5% of the points (going from innermost to outermost contour) for the grey points instead of every point. We also include histograms of $\sigma_{\text{CDPP},4.5\text{hr}}$ and $R_\star \sigma_{\text{CDPP},4.5\text{hr}}$ on top of their respective panels, split into our bluer and redder halves (including all stars regardless of whether they host planets or not, i.e. the grey points). While there is a large scatter in $\sigma_{\text{CDPP},4.5\text{hr}}$ at any given $b_p - r_p$ (left-hand panel), it is clear that the lowest $\sigma_{\text{CDPP},4.5\text{hr}}$ stars are the bluer stars. There is a difference in the distributions of $\sigma_{\text{CDPP},4.5\text{hr}}$ for our bluer and redder samples, which shows that the distribution shifts to larger values for redder stars thus compromising our ability to recover transit signals in the *Kepler* photometry of the redder sample of target stars. Multiplying $\sigma_{\text{CDPP},4.5\text{hr}}$ by the stellar radii (right-hand panel) only partially offsets this bias, suggesting that the net result is that *Kepler* is somewhat more sensitive to planets of a given size in the bluer sample than in the redder sample.

4.3 Are orbital eccentricities correlated with stellar type?

In order to briefly explore correlations between stellar type and other parameters in our model, we also test a model in which the eccentricity scale σ_e is allowed to vary as a function of $b_p - r_p$. For simplicity, we also assume a linear relation parametrized by a slope $d\sigma_e/d(b_p - r_p)$ and y-intercept $\sigma_{e,\text{med}}$ (at median colour, $b_p - r_p \simeq 0.95$; analogous to the form of equation 1). All the model parameters are then re-fit using the same procedure as described in §2, except when computing the distance, we use the circular-normalized transit duration ($t_{\text{dur}}/t_{\text{circ}}$) in place of the transit duration (t_{dur}). The distribution of circular-normalized transit durations is more sensitive to the intrinsic eccentricity distribution once stellar properties are well characterized. We allow for $d\sigma_e/d(b_p - r_p)$ to vary between $[-0.1, 0.1]$ and $\sigma_{e,\text{med}}$ between $[0, 0.1]$. We find no clear trend between σ_e and $b_p - r_p$ in this analysis; while $\sigma_{e,\text{med}}$ is constrained to similarly low values of ~ 0.03 , the slope $d\sigma_e/d(b_p - r_p)$ takes on both positive and negative values. Interestingly, there

appears to be a slight preference for positive or negative slopes compared to zero slope. We interpret this as suggesting that there is evidence for a higher-eccentricity population of exoplanets, but that this is not dependent on the host star color.

4.4 Other correlations in planetary system architectures with stellar type

The models presented in Paper I and in this paper are driven by fits to the marginal distributions of a collection of key observables for the *Kepler* DR25 catalogue of exoplanet candidates, as listed in §2.2.1. As discussed in §2.2, this study adopted a distance function that incorporates simultaneous fits to these summary statistics in the total, bluer, and redder samples in order to infer the best-fitting model parameters. While we assumed the same distribution of planets in each planetary system across all spectral types for the models in this paper, we can examine the fits to the observed data in order to discern possible differences in their architectures.

We plot the results of our best-fitting model (with the model parameters listed in Table 3) in Figure 6, where the model and the data are split into the bluer and redder halves. The panels from top to bottom show the observed distributions of multiplicities (m), orbital periods (P), period ratios (\mathcal{P}), transit depths (δ), transit depth ratios (δ_{i+1}/δ_i), transit durations (t_{dur}), and period-normalized transit duration ratios ($\log \xi$). In the left-hand panels, the solid lines show the distributions for one simulated catalogue, the dashed lines denote the 68.3% credible interval (in each histogram bin) from 100 simulated catalogues passing the (KS) distance threshold, and the shaded histograms show the *Kepler* population given our sample. In the right-hand panels, the cumulative distribution functions (CDFs) are plotted for the simulated catalogue (solid lines) and the data (dashed lines), with the relevant (unweighted) distances shown in the lower-right corners. Figures A2 and A3 in the Appendix show how 10^3 simulated catalogues passing the distance thresholds for KS and AD, respectively, compare to the *Kepler* catalogue in terms of the individual (weighted) distance terms.

Overall, our linear $f_{\text{swpa}}(b_p - r_p)$ model provides an excellent fit to the marginal distributions of the observed *Kepler* planet candidates, for both the bluer and redder samples as well as the combined sample. The best distances are as low as $\mathcal{D}_{W,\text{KS}} \simeq 10$ in both the bluer and redder samples and $\mathcal{D}_{W,\text{KS}} \simeq 12$ for the total sample; for comparison, a “perfect” model would result in $\mathcal{D}_{W,\text{KS}} \simeq 9$ for each of these samples given our number of distance terms. While many of the marginal distributions are fit near perfectly (i.e. have individual weighted distances around unity, given Monte Carlo noise), there are some differences between the *Kepler* data and our model predictions, both subtle and significant (e.g. the transit depth and depth ratio distributions). The bulk of the period distribution is well modelled, although there is a deviation at short periods suggesting a need for a more complicated model than the single power-law we have adopted, perhaps one with a break at ~ 10 d (e.g., Howard et al. 2012; Mulders, Pascucci, & Apai 2015; Mulders et al. 2018). There are fewer planets at the shortest period bins we investigated (~ 3 d) around the bluer stars than the redder stars and the fit to the period distribution is worse, suggesting that the inner edge of planetary systems may be stellar dependent as also found by Plavchan, Bilinski, & Currie (2014); Mulders, Pascucci, & Apai (2015). The fit to the period ratios in our bluer sample is also slightly worse, although the nature of this difference is unclear. On the other hand, the transit depth distribution is very different between our two stellar samples as expected due to the different distributions of stellar radii and photometric precision, but the fit to the redder half is

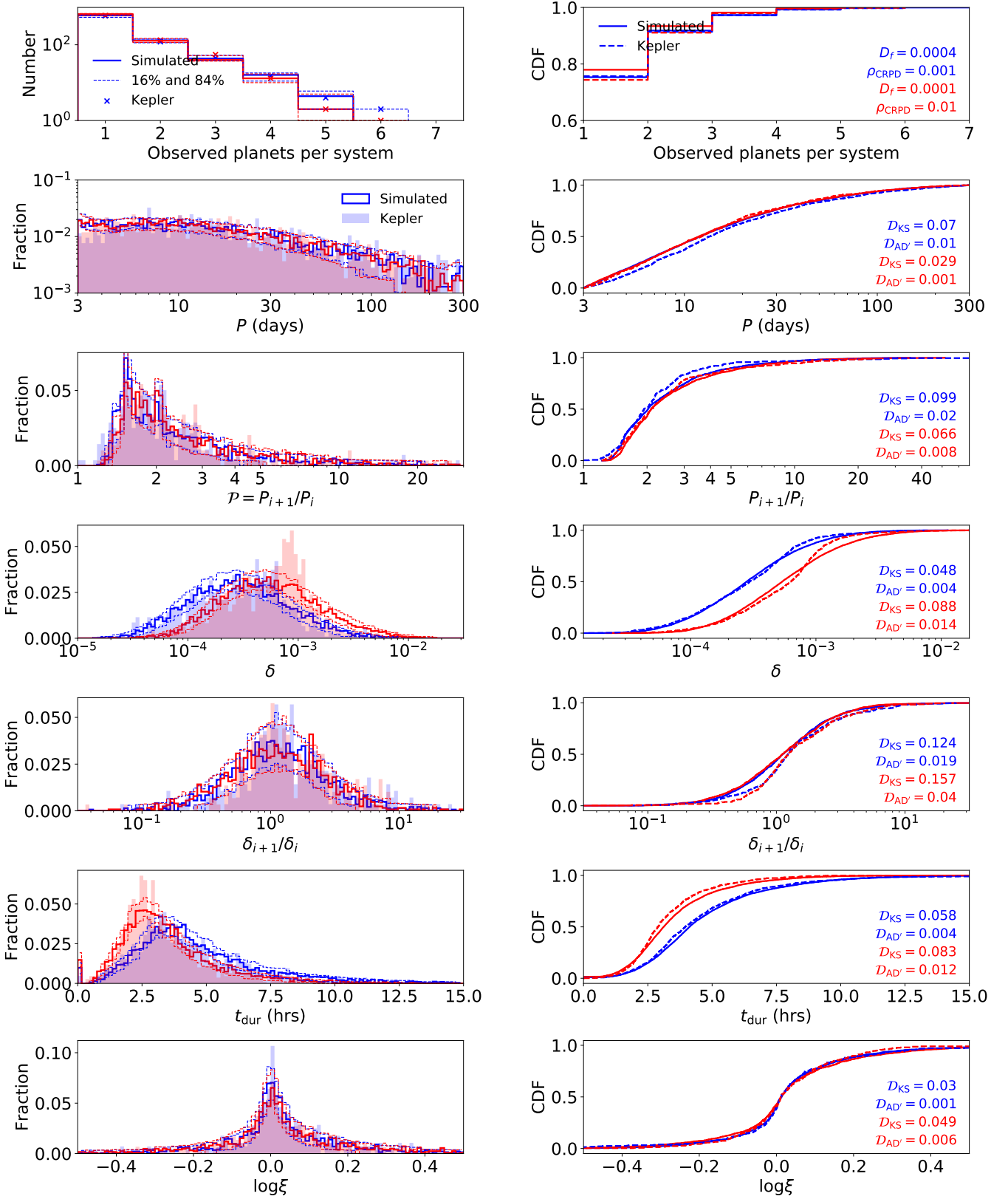


Figure 6. The marginal distributions of the observable properties for our clustered model with linear $f_{\text{swpa}}(b_p - r_p)$ as compared to the *Kepler* data, split into bluer and redder halves as likewise coloured. **Left-hand panels:** histograms of these observables, as labeled. The solid bold lines show one simulated observed catalogue from this model (with parameter values listed in Table 3), while the *Kepler* DR25 exoplanets are plotted as shaded, filled histograms for comparison. The dashed lines show the 16 and 84 percentiles of each bin based on 100 simulated catalogues with parameters drawn from our emulator with $\mathcal{D}_{W, \text{KS}} \leq 40$. **Right-hand panels:** the corresponding CDFs to the left-hand panels. The solid bold lines show the one simulated catalogue, while the dashed lines show the *Kepler* distributions. The relevant KS and AD distances (unweighted) are shown in each panel.

clearly worse than that of the bluer half due to an apparent excess of transit depths at $\sim 10^{-3}$ in the data. The transit depth ratio distribution is very similar between the two stellar samples (in both the data and our model). As in Paper I, we note that while our simple clustering in planet sizes is necessary to explain the highly peaked nature of the distribution, it is not sufficient to explain the asymmetry caused by larger planets being more often the outer planet in observed adjacent pairs (Ciardi et al. 2013; Weiss et al. 2018a; Gilbert & Fabrycky, private communication). The intrinsic planet radius distribution is sculpted by the processes of photoevaporation (Owen & Wu 2013; Fulton et al. 2017; Owen & Wu 2017; Van Eylen et al. 2017; Carrera et al. 2018) and/or heating from formation (e.g. core-powered mass-loss; Ginzburg, Schlichting, & Sari 2016, 2018; Gupta & Schlichting 2018), which our broken power-law with clustering for planet sizes cannot fully encapsulate. The transit duration distributions differ between the bluer and redder halves due to the dependencies on stellar radius and density. While both our constant and linear f_{swpa} models fit the duration distribution for the bluer half slightly better than the redder half, we note that the linear $f_{\text{swpa}}(b_p - r_p)$ model significantly improves the fit to the overall distribution than the baseline model (especially in AD distance). This is easily explained by the overall better matches to the frequency of observed planets of the bluer and redder halves in our linear $f_{\text{swpa}}(b_p - r_p)$ model. Individually, the bluer and redder halves do not improve much with this model, since the system architectures in both models are the same, so we are assigning the same planets around the same stars leading to relatively unchanged individual distributions of t_{dur} . However, the combined distribution changes because the relative contributions of the bluer and redder samples have changed; the constant f_{swpa} model provides too many planets around the bluer stars, which have a different distribution than that of the planets around the redder stars, while the linear $f_{\text{swpa}}(b_p - r_p)$ model provides just the right contributions. Finally, we see no difference in the fits to the period-normalized transit duration ratio distributions, which are modelled extremely well.

5 CONCLUSIONS

We have extended our forward modelling methodology from He, Ford, & Ragozzine (2019) (Paper I) to explore how the occurrence of planetary systems and their architectures may vary as a function of their host stars, using the *Gaia* DR2 $b_p - r_p$ colors as a proxy for stellar effective temperature (i.e. spectral type). We use the same stellar catalog (a clean sample of 79,935 FGK dwarfs as defined in Hsu et al. 2019) and planet catalog (*Kepler* DR25 candidates with periods between [3, 300] d and radii between [0.5, 10] R_{\oplus}) from Paper I, and define f_{swpa} to refer to the fraction of stars that host at least one planet in this range.

First, we adopt the clustered periods and sizes model from Paper I and re-parametrize the intrinsic multiplicity distribution by decoupling the fraction of stars with planets (f_{swpa}) from the numbers of clusters and planets per cluster, to form our baseline model. We show that this does not change our main results about the architectures of planetary systems, namely the underlying power-laws for the period and radius distributions, the extent of intra-cluster similarity in periods and planet radii, the need for two populations of multi-planet systems with different mutual inclination scales in order to explain the observed *Kepler* dichotomy, and the overall f_{swpa} marginalized over all FGK stars.

Then, we generalize our baseline clustered model to include a linear dependence on the spectral type for the fraction of stars with

planets, $f_{\text{swpa}}(b_p - r_p)$. By splitting our stellar sample of FGK stars into two halves (bluer and redder) based on their $b_p - r_p$ colors, modifying our distance function to fit to the observed marginal distributions of both halves and the overall sample, and performing model inference using ABC, we find the following results:

- The observed planet multiplicities in the range we explored are also roughly split in half between our bluer and redder samples. A combination of observational biases (arising from differing stellar properties, photometric precision, etc.) and intrinsic planet occurrence rates conspire to give these near-even numbers of planets.
- Planets of a given size are easier to detect around earlier type (hotter and bluer) stars in the *Kepler* mission. This is mainly due to the improved photometric precision of *Kepler* for these stars as compared to that of the later type stars. Assuming a constant rate of planetary systems across all stars (i.e., our baseline model) produces more detected planets in the bluer sample and fewer in the redder sample than what the *Kepler* data suggests (the roughly even split).
- The two points above imply that the fraction of stars with planets increases towards later type dwarfs (cooler and redder stars). This primary result is in agreement with the general trends reported in Howard et al. (2012) and Mulders, Pascucci, & Apai (2015). Assuming a linear trend, we find a significant positive slope: $df_{\text{swpa}}/d(b_p - r_p) = 0.53^{+0.19}_{-0.19}$ ($0.62^{+0.17}_{-0.19}$) using KS (AD) analyses. This implies that there is a substantial difference in the fraction of stars hosting planetary systems across FGK stars: $f_{\text{swpa}} = 0.34^{+0.08}_{-0.11}$ for F2V dwarfs and $f_{\text{swpa}} = 0.91^{+0.09}_{-0.18}$ for mid K dwarfs. The solar value is roughly half; $f_{\text{swpa}} = 0.54^{+0.08}_{-0.13}$ for G2V. While our linear relation is likely an oversimplification at the extreme ends of our sample, extrapolating to later type stars implies that planetary systems are ubiquitous around M-dwarfs.
- The parameters for the architectures do not change significantly when including a (linear) stellar dependence in our clustered model. Our constant f_{swpa} and linear $f_{\text{swpa}}(b_p - r_p)$ models result in similar rates of clusters and planets, period and radius distributions, eccentricity scales, and evidence for two populations of mutual inclinations.
- Our clustered model with the linear form of $f_{\text{swpa}}(b_p - r_p)$ fits the observed planet multiplicity distributions in our bluer and redder samples extremely well. However, there may be hints of slight differences in the planetary system architectures across spectral types, namely at the inner edges of planetary systems (the period distribution) and in the distribution of planet sizes (the transit depth distribution).
- We find no clear correlation between orbital eccentricity σ_e and spectral type, although there may be some evidence for a population of planets with more highly eccentric orbits than our single Rayleigh distribution with $\sigma_e \approx 0.02$.

Our findings have consequences for informing future follow-up observations of exoplanet detections from the Transiting Exoplanet Survey Satellite (TESS) mission, which is currently in its two-year primary mission (Ricker et al. 2015; Sullivan et al. 2015; Stassun et al. 2018) and is poised for extended missions (Bouma et al. 2017; Huang et al. 2018). With already over a thousand planet candidates collected, the TESS mission is expected to discover many more short-period (~ 10 d) planets around nearby stars which are most amenable to RV follow-up (Barclay, Pepper, & Quintana 2018; Stassun et al. 2018). Being a magnitude limited survey, the TESS mission will observe many more brighter targets (e.g. F stars, compared to later types) in its full field images. Our results show that while these nearby bright stars may be more tenable for transit re-

covery, the intrinsic rate of inner planetary systems is relatively low for these bluer stars and increases significantly towards later type stars. Thus, follow-up efforts should also target these fainter stars as multi-planet systems around such hosts are common. In any case, the primary and extended missions of TESS will likely boost our catalogues of planet candidates around a wide variety of stellar types, further enabling new studies on the architectures of planetary systems as a function of host star properties.

The new catalogs generated from our models are available to the public, along with the core SysSim code (<https://github.com/ExoJulia/ExoplanetsSysSim.jl>), inputs collated from numerous data files (<https://github.com/ExoJulia/SysSimData>), and the code specific to the clustered models (<https://github.com/ExoJulia/SysSimExClusters>). We encourage other researchers to contribute model extensions via Github pull requests and/or additional public git repositories.

ACKNOWLEDGEMENTS

We thank the entire *Kepler* team for years of work leading to a successful mission and data products critical to this study. We acknowledge many valuable contributions with members of the *Kepler* Science Team's working groups on multiple body systems, transit timing variations, and completeness working groups. We thank Keir Ashby, Danley Hsu, and Robert Morehead for contributions to the broader SysSim project. We thank Derek Bingham, Earl Lawrence, Ilya Mandell, Dan Fabrycky, Gregory Gilbert, Jack Lissauer, and Gijs Mulders. M.Y.H. acknowledges the support of the Natural Sciences and Engineering Research Council of Canada (NSERC), funding reference number PGSD3 - 516712 - 2018. E.B.F. and D.R. acknowledge support from NASA Origins of Solar Systems grant # NNX14AI76G and Exoplanet Research Program grant # NNX15AE21. M.Y.H. and E.B.F. acknowledge support from the Penn State Eberly College of Science and Department of Astronomy & Astrophysics, the Center for Exoplanets and Habitable Worlds, and the Center for Astrostatistics. E.B.F. acknowledges support and collaborative scholarly discussions during residency at the Research Group on Big Data and Planets at the Israel Institute for Advanced Studies. The citations in this paper have made use of NASA's Astrophysics Data System Bibliographic Services. This research has made use of the NASA Exoplanet Archive, which is operated by the California Institute of Technology, under contract with the National Aeronautics and Space Administration under the Exoplanet Exploration Program. This work made use of the stellar catalog from [Hsu et al. \(2019\)](#) and thus indirectly the *gaia-kepler.fun* crossmatch database created by Megan Bedell. Several figures in this manuscript were generated using the *corner* .py package ([Foreman-Mackey 2016](#)). We acknowledge the Institute for Computational and Data Sciences (<http://ics.psu.edu/>) at The Pennsylvania State University, including the CyberLAMP cluster supported by NSF grant MRI-1626251, for providing advanced computing resources and services that have contributed to the research results reported in this paper. This study benefited from the 2013 SAMSI workshop on Modern Statistical and Computational Methods for Analysis of *Kepler* Data, the 2016/2017 Program on Statistical, Mathematical and Computational Methods for Astronomy, and their associated working groups. This material was based upon work partially supported by the National Science Foundation under Grant DMS-1127914 to the Statistical and Applied Mathematical Sciences Institute (SAMSI). Any opinions, findings, and

conclusions or recommendations expressed in this material are those of the author(s) and do not necessarily reflect the views of the National Science Foundation.

REFERENCES

- Anderson, T. W. & Darling, D. A. 1952, *The Annals of Mathematical Statistics*, 23, 193
- Barclay, T., Pepper, J., & Quintana, E. V. 2018, *ApJS*, 239, 2
- Batalha, N. M., Rowe, J. F., Bryson, S. T., et al. 2013, *ApJS*, 204, 24
- Borucki, W. J., Koch, D. G., Basri, G., et al. 2010, *Science*, 327, 977
- Borucki, W. J., Koch, D. G., Basri, G., et al. 2011a, *ApJ*, 728, 117
- Borucki, W. J., Koch, D. G., Basri, G., et al. 2011b, *ApJ*, 736, 19
- Bouma, L. G., et al. 2017, arXiv:1705.08891
- Bryson, S. 2020 *Res. Notes AAS*, 4, 32
- Burke, C. J., & Catanzarite, J. 2017a, *Planet Detection Metrics: Window and One-Sigma Depth Functions for Data Release 25*, Tech. rep.
- Burke, C. J., & Catanzarite, J. 2017b, *Planet Detection Metrics: Per-Target Flux-Level Transit Injection Tests of TPS for Data Release 25*, Tech. rep.
- Burke, C. J., & Catanzarite, J. 2017c, *Planet Detection Metrics: Per-Target Detection Contours for Data Release 25*, Tech. rep.
- Carrera, D., Ford, E. B., Izidoro, A., et al. 2018, *ApJ*, 866, 104
- Catanzarite, J. & Shao, M. 2011, *ApJ*, 738, 151
- Christiansen, J. L., Jenkins, J. M., Caldwell, D. A., et al. 2012, *PASP*, 124, 1279
- Christiansen, J. L. 2017, *Planet Detection Metrics: Pixel-Level Transit Injection Tests of Pipeline Detection Efficiency for Data Release 25*, Tech. rep.
- Ciardi, D. R., Fabrycky, D. C., Ford, E. B., et al. 2013, *ApJ*, 763, 41
- Coughlin, J. L. 2017, *Planet Detection Metrics: Robovetter Completeness and Effectiveness for Data Release 25*, Tech. rep.
- Cressie, N. & Read, T. R. C. 1984, *Journal of the Royal Statistical Society. Series B*, 46, 440
- Dressing, C. D. & Charbonneau, D. 2013, *ApJ*, 767, 95
- Fabrycky, D. C., Lissauer, J. J., Ragozzine, D., et al. 2014, *ApJ*, 790, 146
- Ford, E. B., He, M. Y., Hsu, D. C., & Ragozzine, D. 2018b, *Planetary Systems Simulation & Model of Kepler Mission for Characterizing the Occurrence Rates of Exoplanets and Planetary Architectures*, v1.0, Zenodo, doi:10.5281/zenodo.1205172. <https://doi.org/10.5281/zenodo.1205172>
- Foreman-Mackey, D. 2016, *corner.py: Scatterplot matrices in Python*, *Journal of Open Source Software*, 1(2), 24, doi:10.21105/joss.00024
- Fressin, F., Torres, G., Charbonneau, D., et al. 2013, *ApJ*, 766, 81
- Fulton, B. J., Petigura, E. A., Howard, A. W., et al. 2017, *AJ*, 154, 109
- Gaia Collaboration, Brown, A. G. A., Vallenari, A., et al. 2018, *A&A*, 616, A1
- Gaidos, E., Mann, A. W., Kraus, A. L., et al. 2016, *MNRAS*, 457, 2877
- Ginzburg, S., Schlichting, H. E., & Sari, R. 2016, *ApJ*, 825, 29
- Ginzburg, S., Schlichting, H. E., & Sari, R. 2016, *MNRAS*, 476, 759
- Gupta, A. & Schlichting, H. E. 2018, *Sculpting the Valley in the Radius Distribution of Small Exoplanets as a by-product of Planet Formation: The Core-Powered Mass-Loss Mechanism*, arXiv:1811.03202
- Hardegree-Ullman, K. K., Cushing, M. C., Muirhead, P. S., & Christiansen, J. L. 2019, *AJ*, 158, 75
- He, M. Y., Ford, E. B., & Ragozzine, D. 2019, *MNRAS*, 490, 4575
- Howard, A. W., Marcy, G. W., Bryson, S. T., et al. 2012, *ApJS*, 201, 15
- Hsu, D. C., Ford, E. B., Ragozzine, D., et al. 2018, *AJ*, 155, 205
- Hsu, D. C., Ford, E. B., Ragozzine, D., & Ashby, K. 2019, *AJ*, 158, 109
- Hsu, D. C., Ford, E. B., & Terrien, R. 2020, *Occurrence Rates of Planets Orbiting M Stars: Applying ABC to Kepler DR25, Gaia DR2, and 2MASS Data*, arXiv:2002.02573
- Huang, C. X., Shporer, A., Dragomir, D., et al. 2018, *Expected Yields of Planet Discoveries from the TESS primary and extended missions*, arXiv:1807.11129
- Kolmogorov, A. N. 1933, *Giornale dell'Istituto Italiano degli Attuari*, 4, 83
- Latham, D. W., Rowe, J. F., Quinn, S. N., et al. 2011, *ApJL*, 732, L24

- Lissauer, J. J., Fabrycky, D. C., Ford, E. B., et al. 2011a, *Nature*, 470, 53
- Lissauer, J. J., Ragozzine, D., Fabrycky, D. C., et al. 2011b, *ApJS*, 197, 8
- Lissauer, J. J., Marcy, G. W., Bryson, S. T., et al. 2014, *ApJ*, 784, 44
- Mulders, G., Pascucci, I., & Apai, D. 2015, *ApJ*, 798, 112
- Mulders, G. D., Pascucci, I., Apai, D., et al. 2018, *AJ*, 156, 24
- Ning, B., Wolfgang, A., & Ghosh, S. 2018, arXiv:1811.02324
- Owen, J. E. & Wu, Y. 2013, *Kepler Planets: A Tale of Evaporation*, *ApJ*, 775, 105
- Owen, J. E. & Wu, Y. 2017, *ApJ*, 847, 29
- Pecaut, M. J. & Mamajek, E. E. 2013, *ApJS*, 208, 9
- Petigura, E. A., Marcy, G. W., & Howard, A. W. 2013b, *ApJ*, 770, 69
- Pettitt, A. N. 1976, *Biometrika*, 63, 161
- Plavchan, P., Bilinski, C., & Currie, T. 2014, *PASP*, 126, 935
- Pu, B. & Wu, Y. 2015, *ApJ*, 807, 44
- Ragozzine, D. & Holman, M. J. 2010, arXiv:1006.3727
- Rasmussen, C. E. & Williams, C. K. I. 2006, *Gaussian Processes for Machine Learning*, MIT Press, ISBN 0-262-18253-X
- Ricker, G. R., Winn, J. N., Vanderspek, R., et al. 2015, *JATIS*, 1, 014003
- Rowe, J. F., Bryson, S. T., Marcy, G. W., et al. 2014, *ApJ*, 784, 45
- Rowe, J. F., Coughlin, J. L., Antoci, V., et al. 2015, *ApJS*, 217, 16
- Sandford, E., Kipping, D., & Collins, M. 2019, *MNRAS*, 489, 3162
- Smirnov, N. 1948, *The Annals of Mathematical Statistics*, 19, 279
- Stassun, K. G., Oelkers, R. J., Pepper, J., et al. 2018, *AJ*, 156, 102
- Steffen, J. H., Batalha, N. M., Borucki, W., J., et al. 2010, *ApJ*, 725, 1226
- Sullivan, P. W., Winn, J. N., Berta-Thompson, Z. K., et al. 2015, *ApJ*, 809, 77
- Thompson, S. E., Coughlin, J. L., Hoffman, K., et al. 2018, *ApJS*, 235, 38
- Van Eylen, V. & Albrecht, S. 2015, *ApJ*, 808, 126
- Van Eylen, V., Agentoft, C., Lundkvist, M. S., et al. 2018, *MNRAS*, 479, 4786
- Weiss, L. M., Marcy, G. W., Petigura, E. A., et al. 2018, *AJ*, 155, 48
- Winn, J. N. & Fabrycky, D. C. 2015, *ARAA*, 53, 407
- Yang, J.-Y., Xie, J.-W., & Zhou, J.-L. 2020, arXiv:2002.02840
- Zhu, W., Petrovich, C., Wu, Y., et al. 2018, *ApJ*, 860, 101

This paper has been typeset from a $\text{\TeX}/\text{\LaTeX}$ file prepared by the author.

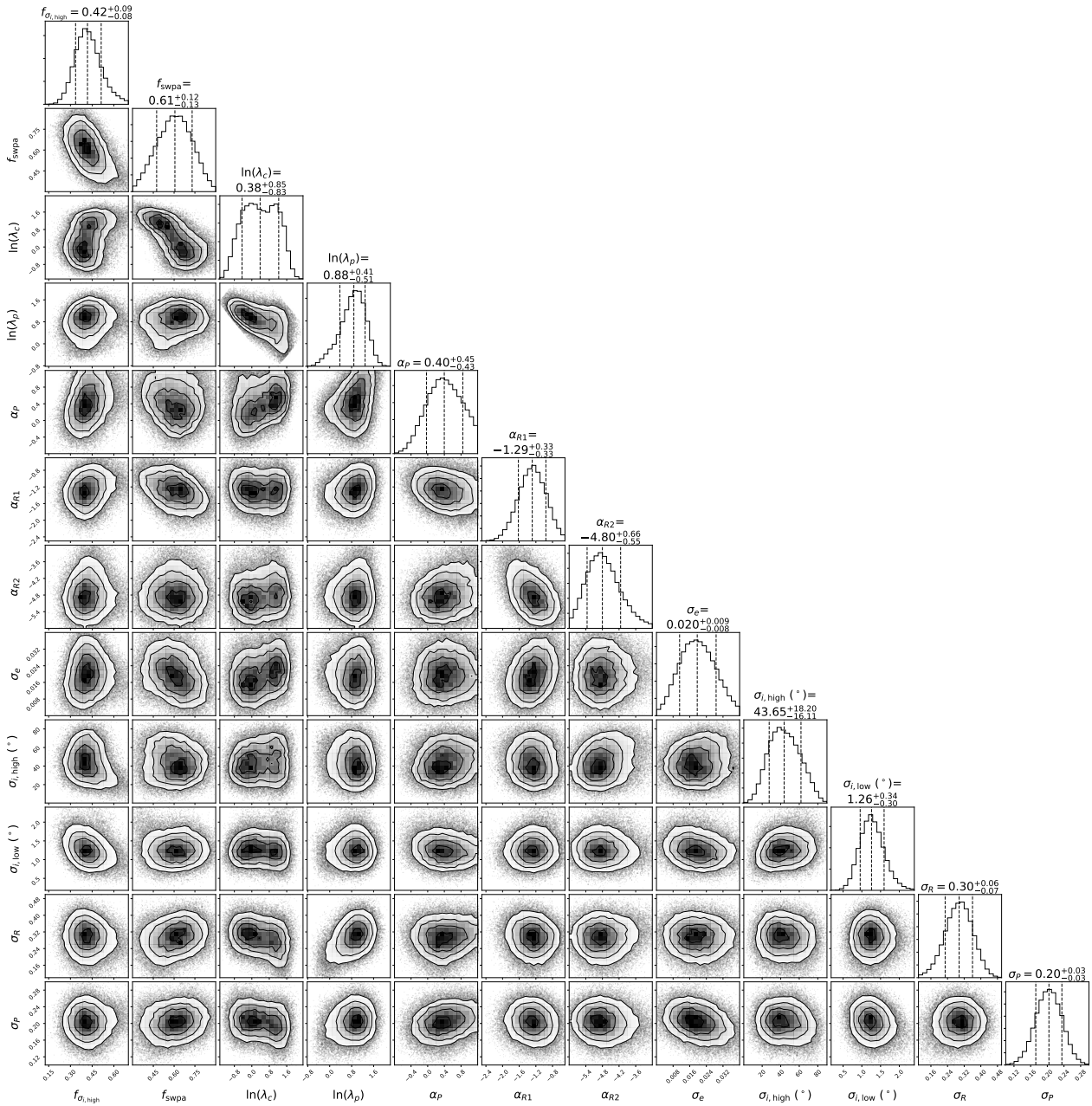


Figure A1. The ABC posterior distributions of the free model parameters of the clustered model with constant f_{swpa} . A total of 5×10^4 points passing a distance threshold of $\mathcal{D}_{W, \text{KS}} = 45$ as drawn from the GP emulator are shown. The prior mean function was set to a constant value of 75.

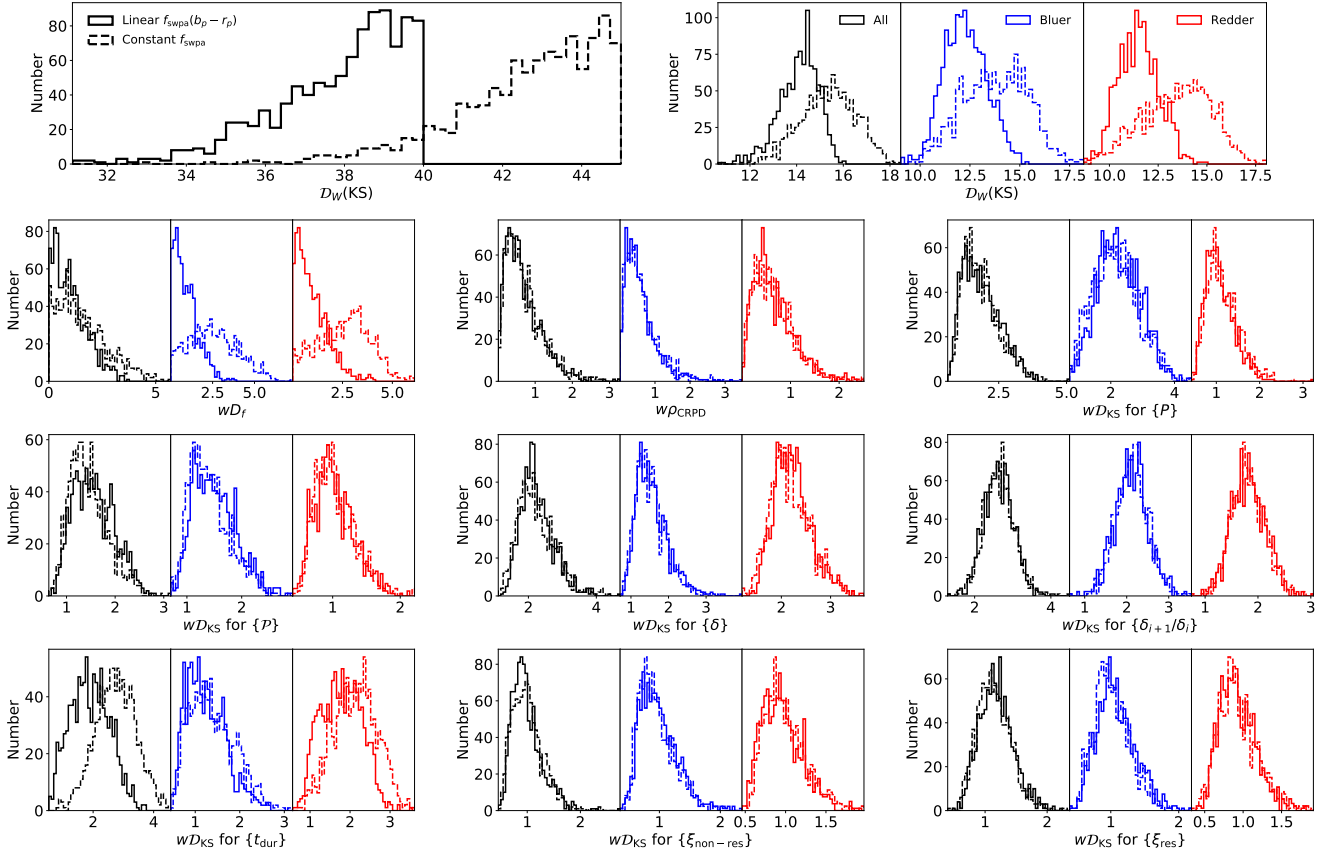


Figure A2. Histograms of the weighted total distances (top row) and individual distance terms (second row and below) for our models as compared to the *Kepler* data, including 1000 simulated catalogues that pass our distance thresholds of $\mathcal{D}_{W,KS} = 45$ and $\mathcal{D}_{W,KS} = 40$ for the constant f_{swpa} (dashed histograms) and linear $f_{swpa}(b_p - r_p)$ (solid histograms) models, respectively. In the top row, the right-hand panel shows the weighted sum of the individual distance terms for each subset (all, bluer, and redder stars in our sample, coloured black, blue, and red, respectively), while the left-hand panel shows the sum of these three components. The panels in the second row and below show the (weighted) individual distance terms for each subset. Note that the x-axes for each subplot are not necessarily the same.

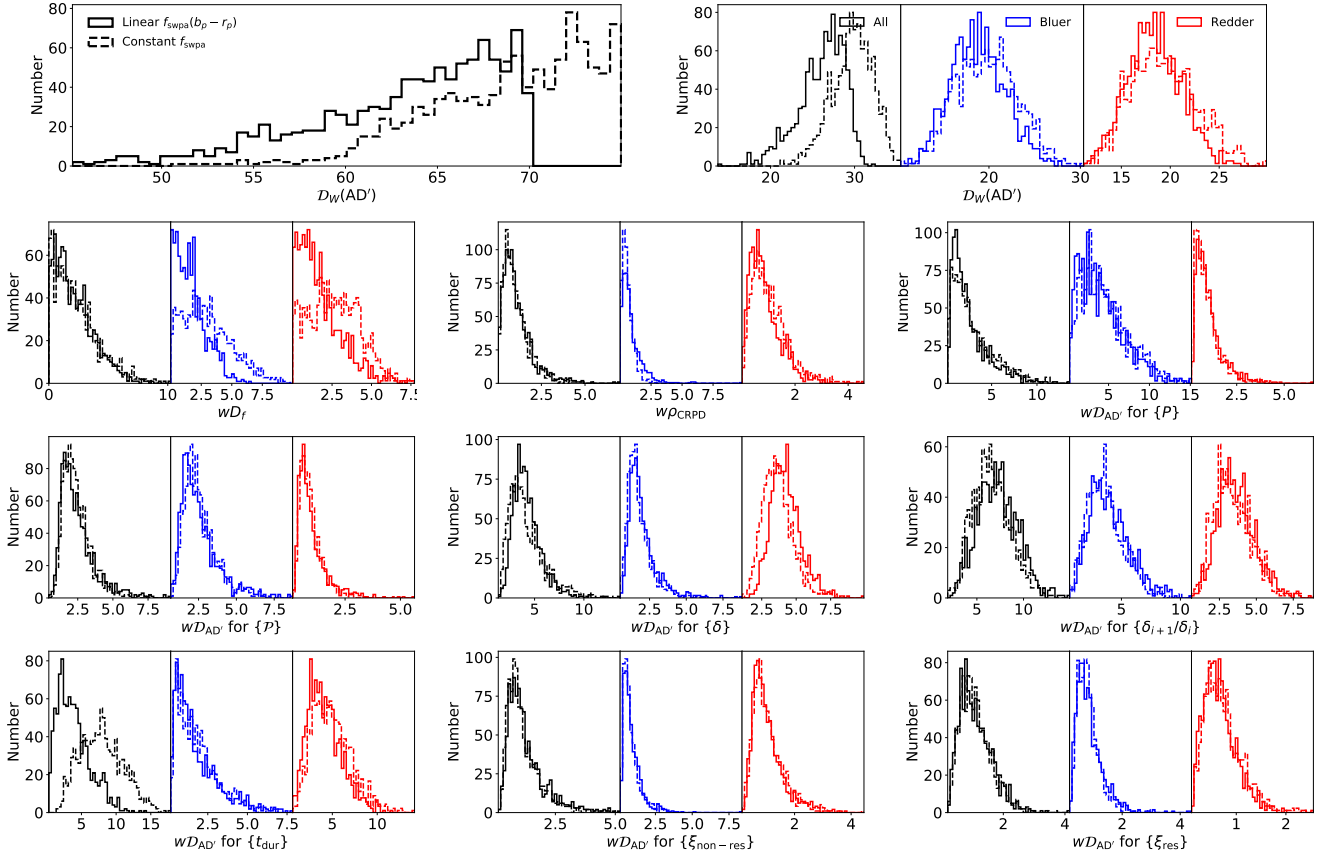


Figure A3. Histograms of the weighted total distances (top row) and individual distance terms (second row and below) for our models as compared to the *Kepler* data, including 1000 simulated catalogues that pass our distance thresholds of $\mathcal{D}_{W,AD'} = 75$ and $\mathcal{D}_{W,AD'} = 70$ for the constant f_{sspa} (dashed histograms) and linear $f_{sspa}(b_p - r_p)$ (solid histograms) models, respectively. The panels, lines, and colours are the same as those in Figure A2.